INVESTIGATION OF THE CURRENT TRANSPORT MECHANISMS IN FIRE THROUGH DIELECTRIC CONTACT (FTDC) TO SILICON SOLAR CELLS BY SPECTROSCOPIC ANALYSES

by

Keming Ren

A dissertation submitted to the faculty of
The University of North Carolina at Charlotte
in partial fulfillment of the requirements
for the degree of Doctor of Philosophy in
Nanoscale Science

Charlotte

2020

Approved by:

_____
Dr. Abasifreke Ebong

_____
Dr. Yong Zhang

_____
Dr. Michael G. Walter

_____
Dr. Haitao Zhang

_____
Dr. Thomas A. Schmedake

ABSTRACT

KEMING REN. Investigation of The Current Transport Mechanisms in Fire Through Dielectric Contact (FTDC) to Silicon Solar Cells by Spectroscopic Analyses.
(Under the direction of DR. ABASIFREKE EBONG)

This thesis work investigates the current transport mechanisms at the Si/gridline interface of the screen-printed commercial silicon (Si) solar cell with lowly doped emitter. The use of lightly doped emitter is one way to improve the efficiency of a Si solar cell. In addition, developing the screen-printable Ag-Cu paste to reduce the cost of using 90-95% Ag powder is crucial to reach the cost-effective solar electricity. Hence, the contacts under investigation are, respectively, Ag/Si and Ag-Cu/Si, which are formed with screen-printable pastes consisting Ag powder (and, or Cu at some $wt\%$), glass frits and organic binders. For screen-printable contacts formed on heavily doped emitter, the contact resistance at the Ag/Si is always low but because of the shadowing and surface recombination losses, the cell efficiency is low. In this work, the Ag/Si interface on lightly doped emitter was first studied to elucidate the understanding of the transport mechanisms at the interface and then was extended to the Ag-Cu/Si interface.

Optical and electrical characterization of the Ag/Si interface was carried out after the contact formation at high temperature. For the Ag/Si interface on the lightly doped emitter, a very thick interface glass layer (IGL) was measured, which should show high contact resistance according to literature. However, in this case, the IGL was found to be conductive according the conductive AFM (c-AFM) I-V curve, which fitted a barrier height of only 0.1 eV. This low barrier height stems from the formation of the semimetal nano-alloys found in the glass layer revealed by Raman Spectrographs. These nano-alloys are low-bandgap compounds, PbTe and Ag_2Te, and could be responsible for the high conductivity exhibited by the thick IGL. Thus, in

the presence of these semimetal alloys, the contact behaves as ohmic as seen with the lithography and buried contacts which are pure metal-semiconductor contacts.

For the Ag-Cu paste contacts, the SEM showed that the glass was first doped with Cu, which led to increased glass frit transition temperature (T_g). Thus, the high glass transition temperature impeded the uniform spreading of the molten glass and resulted in poor wetting and etching of the SiN_x with the agglomerated Ag crystallites found in the Si. Further analysis with STEM showed that the IGL at the Ag-Cu/Si interface acted as an effective diffusion barrier layer to prevent Cu atoms from diffusing into the Si emitter, which is the primary requirement for applying Cu in the Si solar cells. More so, the c-AFM in conjunction with the SEM and STEM analyses revealed that the growth of Ag crystallites in the Si emitter is responsible for carrier conduction in the Ag-Cu contacts.

For the Ag-Cu/Si contact fired at high temperature, Cu tended to dope the glass frit and was sequestered by the resulting oxide. The higher the ratio of Cu to Ag, the thicker the formed oxide. It can therefore, be concluded that, part replacement of Ag with Cu may not be the way to go but it can be the use of Cu paste with 90-95% Cu powder as in the Ag paste, if the paste can be formulated such that Cu does not oxidize in the atmosphere. Thus, the future work focuses on the atmospheric Cu-paste. The preliminary study with the atmospheric Cu paste showed very promising results with the Cu particles being sequestered in the oxide so it does not diffuse into Si. Open circuit voltage of 628 mV and the ideality factor of 1.17 with J_{o2} of $1.1 \times 10^{-8} A/cm^2$ indicate that the p-n junction is not damaged by Cu diffusion.

ACKNOWLEDGEMENTS

TABLE OF CONTENTS

LIST OF FIGURES

LIST OF TABLES

CHAPTER 1: Introduction

1.1   Motivation

The enormous usage of fossil fuel as energy source to meet the increasing energy need has caused extreme anthropogenic emission of greenhouse gases and consequent environment pollution. In this case, an alternative energy source which should be environmentally friendly and renewable is desirable to replace the fossil fuel energy source. Among all renewable energy sources, such as wind, geothermal and hydro-electric, photovoltaic (PV) technology, which is developed to convert solar energy into solar electricity, is projected by the U.S. Energy Information Administration in 2019 [1] that in 2050, solar photovoltaic (PV) will provide 48% of renewable electricity generation, as shown in Figure 1.1. In addition, the Department of Energy announced that the SunShot 2030 goal of utility-scale solar electricity would be $0.03 per kilowatt hour which would make solar electricity to be among the least expensive new power options and to be cheaper than the electricity from most fossil fuels [2]. In order to meet the goal of high solar electricity generation and low-cost solar electricity, the solar cell efficiency should be high and cost effective. As the silicon (Si) solar cells have dominated solar market, and according to the International Technology Roadmap for Photovoltaic (ITRPV) 2019 report [3], the major Si solar cells will still be p-type in the upcoming decade with efficiency approaching $\sim 24\%$, further efforts will be focused on improving the cell efficiency to 24% on the p-type at lower cost.
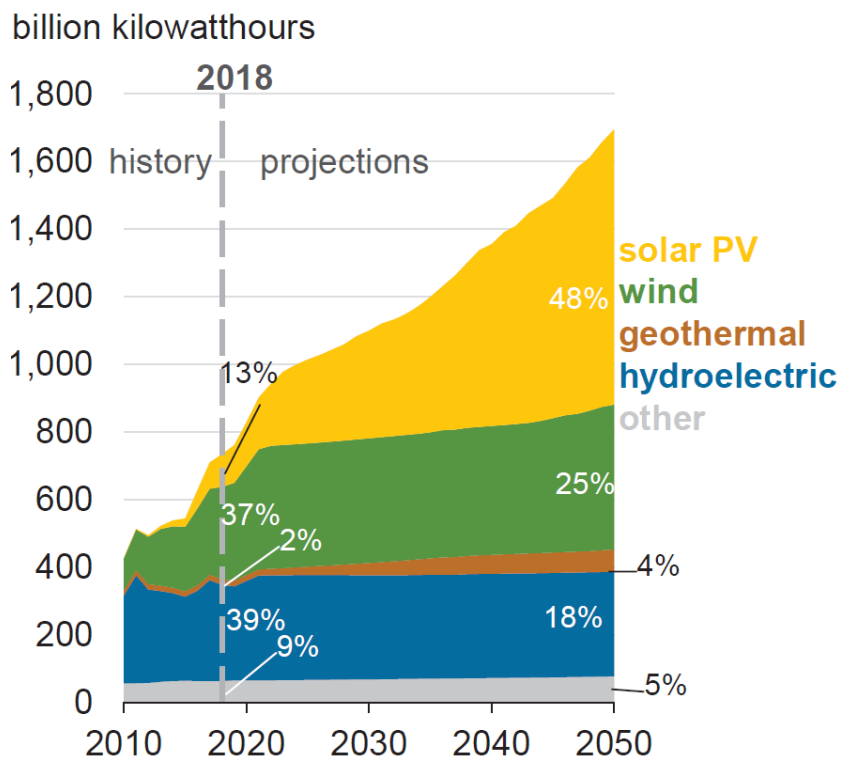
Figure 1.1: Percentages of renewable electricity generation from different sources [1].

1.2 Commercial Si Solar Cells

A typical commercial Si solar cell structure fabricated on p-type crystalline silicon is shown in Figure 1.2. The solar cell is a p-n junction made of phosphorus doped n-type (sunward side) and boron doped p-type as the bulk and metal contacts on both front and back sides. The antireflective coating (ARC) deposited on the sunward side in addition to the surface texturing is to reduce the surface reflection. When the solar cell is exposed to sunlight, photons are absorbed in the p-bulk and the electron-hole pairs are generated. Due to the electric field that exists at the p-n junction resulting from the depletion region, electrons and holes are separated and the current is extracted via the front (electrons) and rear contacts (holes).
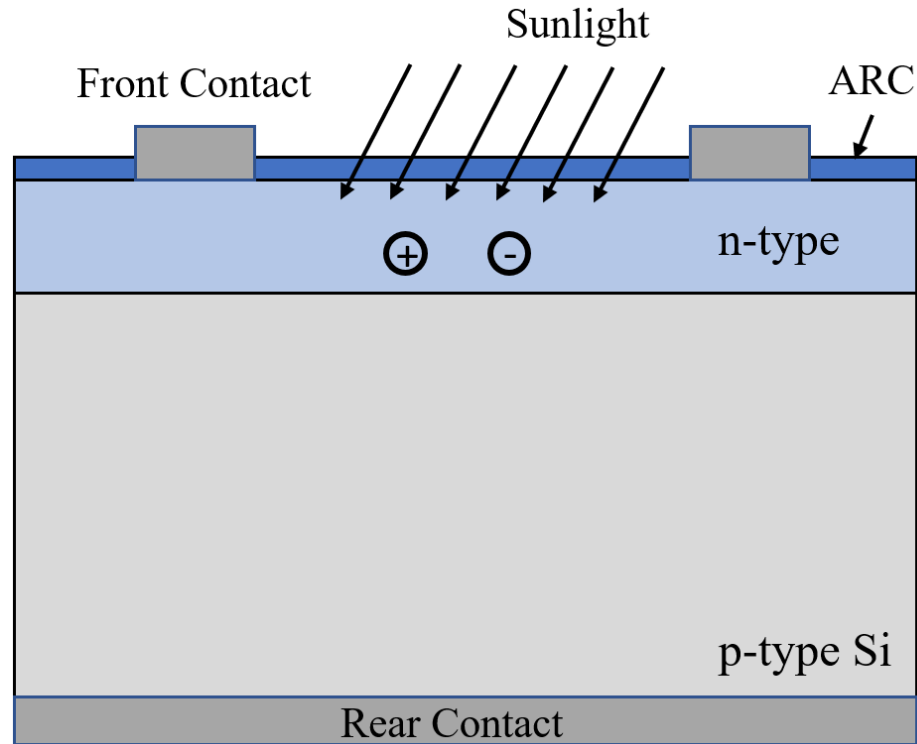
Figure 1.2: Schematic drawing of a solar cell.

Figure 1.3 shows two main structures of commercial Si solar cells which are Aluminum Back Surface Field (Al-BSF) and Passivated Emitter Rear Contact (PERC), respectively. Both cells have the front emitter surface textured and deposited ARC to reduce the optical losses. The front contacts for both cells are same and designed to reduce shading losses and series resistance. The only difference lies on the back contacts. In the Al-BSF cell, the rear side is mainly covered by metal contact (Aluminum), while in the PERC cell, the rear side is passivated and the contacts are fabricated on selected areas to increase rear reflection and to reduce surface recombination.
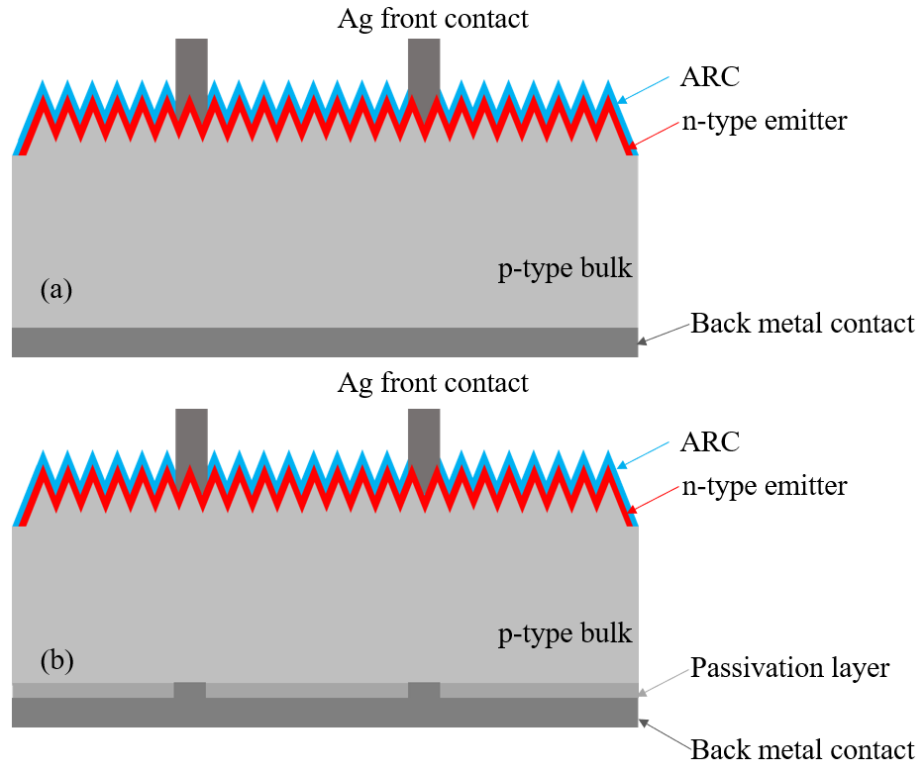
Figure 1.3: Two main types of commercial Si solar cells, (a) Al-BSF cell; (b) PERC cell.

1.2.1 Fabrication of Si Solar Cells

The predominant process steps to fabricate Si solar cells, for example Al-BSF cell, is illustrated in Figure 1.4 which includes seven steps: (1) Saw damage removal and surface texturization are achieved with alkali etchants like NaOH or KOH followed by cleaning steps with $H_2SO_4 + H_2O_2 + H_2O$, $HCl + H_2O_2 + H_2O$, and $HF + H_2O$ to remove organic materials, metal precipitates and remove native SiO_2 layer on the surface, respectively; (2) the n-type emitter is formed by diffusion of phosphorous under high temperature either through N_2 gas transporting $POCl_3$ or printing the diffusion source onto the wafer; (3) remove phosphorus glass and isolate parasitic p-n junctions at the wafer edge by wet chemistry etching; (4) Plasma Enhanced Chemical Vapor Deposition (PECVD) deposits the antireflective coating; (5 & 6) Fire Through Dielectric Contact (FTDC) process is the dominant way for the metallization in Si

solar cells due to its high throughput and simplicity, where the front and back metal contacts are in turn screen printed onto the Si wafer and after dried, are co-fired under peak high temperature for a short time; (7) after cool down, the cell is characterized and ready for use.
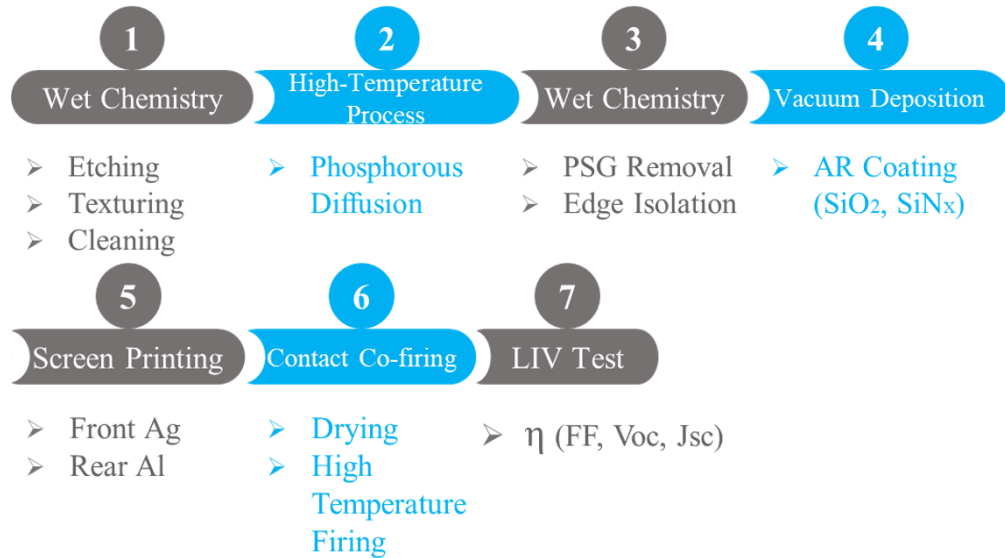
Figure 1.4: Standard industrial Si solar cell fabrication processes.

1.2.2   Screen Printing and Firing

Following the fabrication process steps in Figure 1.4, all samples, included in this dissertation, are prepared on the wafers which already have the first four steps (step 1~4) completed with antireflective coating and are ready for screen printing and firing (step 5 & 6). The screen-printing process (step 5) is demonstrated in Figure 1.5 (a) where the screen is placed above the wafer and the paste is printed onto the wafer when the squeegee moves forward. Figure 1.5 (b) and 1.5 (c) show the screens for printing the front contacts and rear contact, respectively. Figure (d) shows the microstructure of the screen meshed and middle opening area, which allows the paste to go through. Figure 1.5 (e) is the screen printer used by the PV Research Laboratory at the University of North Carolina at Charlotte.
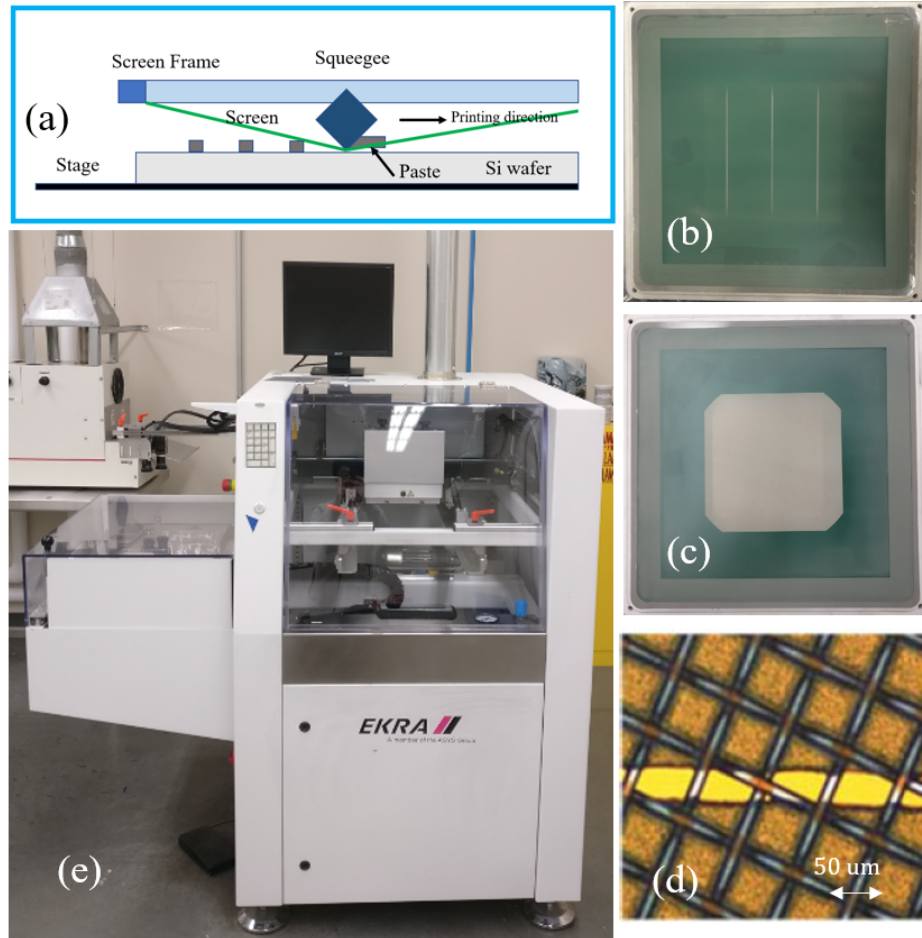
Figure 1.5: (a) screen printing process; screens to print (b) front and (c) rear sides with (d) the top view of the wire mesh; (e) lab printer at the PV Research Laboratory.

Compared with the rear contacts, using Ag paste to print the fine front Ag contacts on the Si wafer is more important because the properties of these Ag contacts impact both the optical loss due to shadowing and electrical loss due to series resistance in the Si solar cell, and hence the cell performance. The quality of the Ag contacts is decided by the Ag paste itself. The components of the Ag paste include: $\sim 90\ wt\%$ Ag powder, $\sim 6\ wt\%$ organic binder and $\sim 4\ wt\%$ glass frits, as show in Figure 1.6.
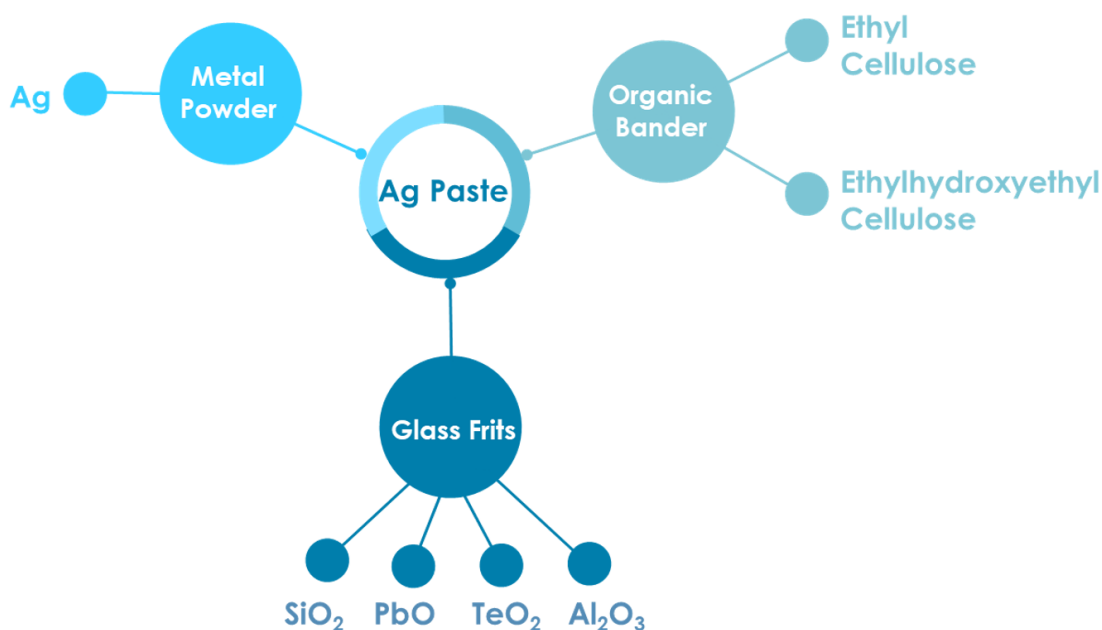
Figure 1.6: Components of commercial Ag paste.

The lab furnace used for firing the Si solar cells (step 6) is shown in Figure 1.7(a) with its thermal profile in Figure 1.7(b). During the firing process, the Si solar cell is heated up to a peak temperature of about 800 ^oC and then quenched to the room temperature. The contact formation mechanism is that (1) at temperature under 400 ^oC, the organic binder evaporates and burns out; (2) before the temperature gets up to 600 ^oC, the glass frits melt and the melted glass wets the emitter surface; (3) above 600 ^oC, the melted glass reacts with SiN_x layer which is the ARC through redox reactions and this allows Ag metal to contact with the Si emitter. The cell will stay under peak temperature for a short time. (4) after that, the cell will cool down quickly to avoid glass over etching Si emitter.
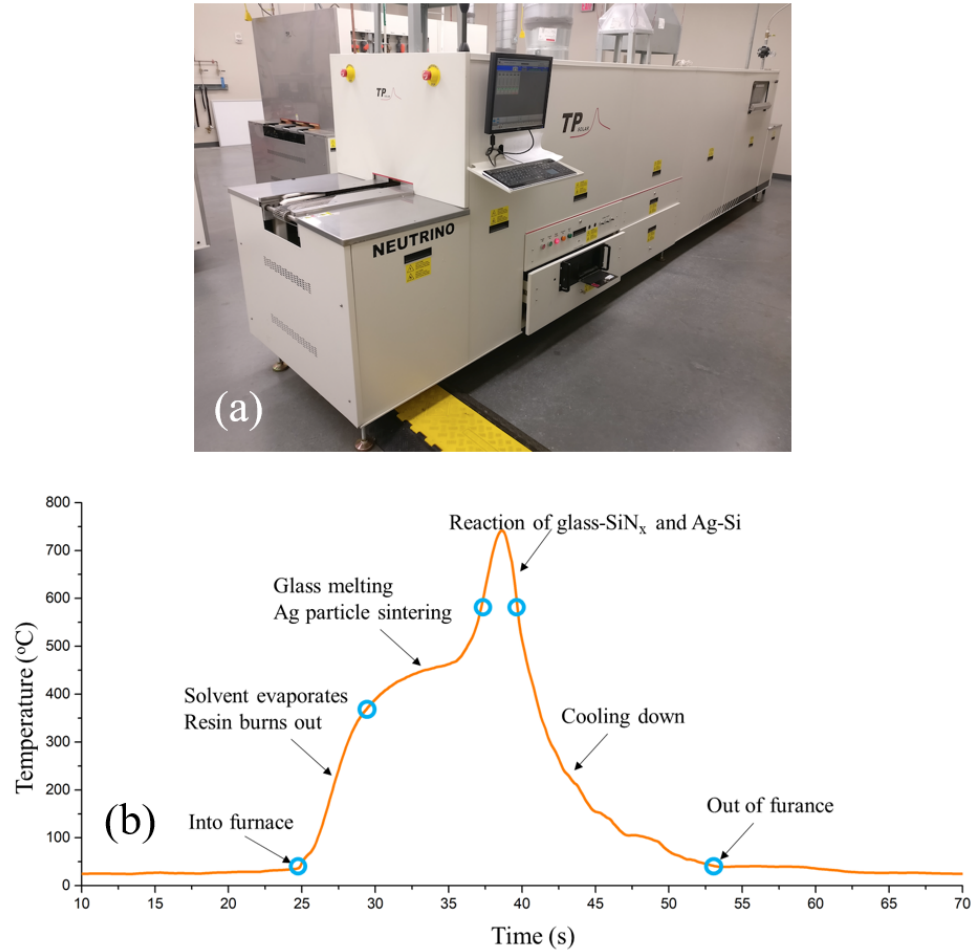
Figure 1.7: (a) the infrared belt furnace at the PV Research Laboratory; (b) thermal profile of the furnace.

In general, solar cell technologies are characterized according to the contacting technique, which includes: lithography, buried contact and fire through. Both lithography and buried contact use selective emitter approach encompassing double diffusion (emitter diffusion and contact diffusion) to isolate the metal contact and reduce metal recombination. The lithography on one hand requires vacuum evaporation or sputtering of the contacts, which include: Ti/Pd/Ag on the front and Al/Ag on the back side, followed by light induced plating of Ag to thicken the gridlines. The buried contact on the other hand uses laser to form the front grooves that is diffused heavier than the emitter before the Ni plating plus anneal at 400oC to form NiSi alloy before Cu plating to fill the grooves and then followed by Ag dip to avoid oxidation

of Cu. The contacts formed here are pure metal contact on semiconductor and it obeys the field emission carrier transport at the interface of the Si/gridline. However, the fire through contact made with screen-printed Ag paste is not pure metal to semiconductor but metal/insulator/semiconductor. Thus, the whole challenge of screen-printing technology is to understand the material interaction at this interface to create a contact that will mimic the lithography and buried contact with simple process exhibiting similar or better result.

1.3   Improvement Strategies

Based on the state-of-the-art fabrication process steps for FTDC, to improve the Si solar cell to be (1) more efficient and (2) less costly, the following strategies are imperative.

(a) Use of emitter sheet resistance of 140 Ω/sq (ITPVR [3]) to take advantage of lower surface recombination and increased blue response [4] to enhance J_{sc} and V_{oc};

(b) Use of narrow gridlines (from 60 um to 20 um) to reduce grid shadowing, decrease silver consumption (50 $mg/cell$ in 2029) and favor J_{sc};

(c) Use of Cu or other low-cost metal without additional process steps and equipment - Cu is a highly conductive metal with conductivity close to that of Ag but 100 times more cost-effective.

1.4   Challenges

Future improvement of p-type Si solar cell will be through the lowly doped emitter with fabrication of narrow Ag contacts, Ag-Cu or Cu contacts. These strategies, ultimately, are about the front metallization which affects the cell efficiency through shadowing related optical losses and series resistance related electrical losses. The shadowing in Si solar cell results from the front metal contacts, blocking the incident light and can be minimized by printing fine lines. The series resistance in the Si solar cell consists of six components as shown in Figure 1.8: (i) back contact, R_1, (ii)

bulk, R_2, (iii) emitter, R_3, (iv) contact, R_4, (v) gridline, R_5 and (vi) busbar, R_6. The application of high sheet resistance emitter leads to higher R_3 which can be reduced by increasing the number of fingers. The front metallization impacts R_4, R_5 and R_6. Among these three components, R_6 is much smaller than R_4 and R_5 due to the larger dimension of busbars and can be optimized through screen design. R_5 is decided by the dimension of fingers and even for fine lines (20 um), R_5 can be reduced through reduction of the finger length by multi-busbar design. However, R_4 is known as the contact resistance (R_c) which is impacted by both emitter doping and the dimensions of the fingers.
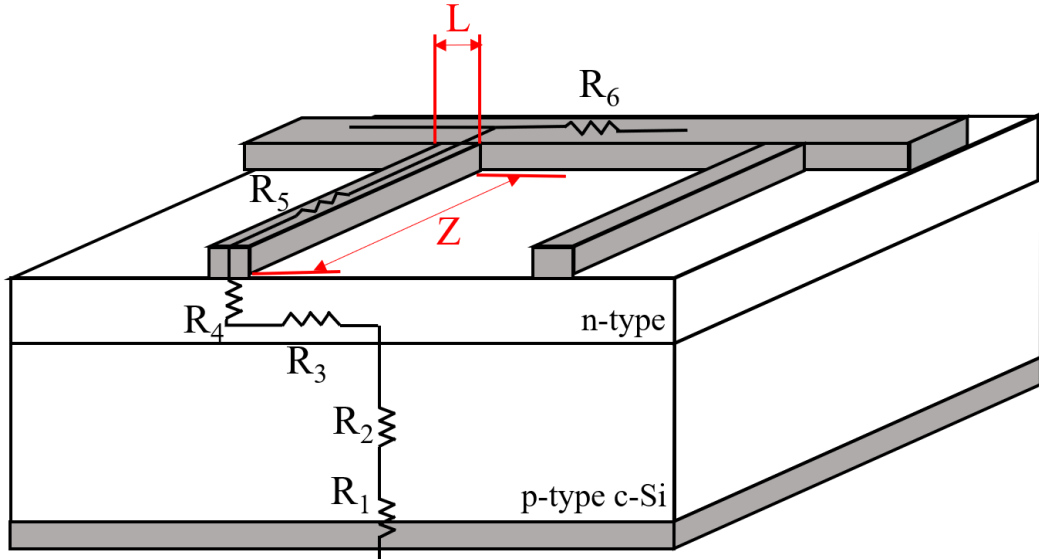
Figure 1.8: Schematic drawing of series resistance sources in an Si solar cell.

According to DK Schroder et al. [5],

$$R_c = (L_T/Z)R_{sheet} \cdot coth(L/L_T) \tag{1.1}$$

where Z is the finger length, L is the finger width, R_{sheet} is the emitter sheet resistance, the L_T is the transfer length and defined by:

$$L_T = \sqrt{\rho_c/R_{sheet}} \tag{1.2}$$

where ρ_c is the specific contact resistance.

The Equation 1.1 is valid for $Z \gg L$ and L_T and for negligible metal resistance.

Two limiting cases of Equation 1.1:

For $L \geq 1.5L_T$,

$$R_c \simeq L_T R_{sheet}/Z = \rho_c/(L_T Z) \tag{1.3}$$

Substituting Equation 1.2 in Equation 1.3 gives

$$R_c \simeq \frac{\sqrt{\rho_c \cdot R_{sheet}}}{Z} \tag{1.4}$$

For $L < 0.5L_T$ or $L < 10$ um for lowly doped emitter,

$$R_c \simeq \rho_c/(LZ) \tag{1.5}$$

According to Equation 1.4 and 1.5, when the finger width (L) is 20 um and the lowly doped emitter has $R_{sheet} = 140$ Ω/sq, the R_c will be mainly decided by ρ_c, because Z can only be slightly changed through multi-busbar design. In addition, R_c increases largely with increasing ρ_c, according to a numerical modeling that increase ρ_c from 10^{-3} Ωcm^2 to 10^{-2} Ωcm^2 caused Rc to increase from 0.3 Ω to 2 Ω [5]. Hence, the ρ_c needs to be low enough to have low R_c and thus low total series resistance.

1.4.1 Specific Contact Resistance

Based on the metal-semiconductor contacts [6, 7], the ρ_c is related to the current flow over the interfacial barrier which has three processes in Figure 8, and relies on the emitter doping concentration (N_D):

(1) Field emission (FE): when 10^{19} $cm^{-3} \leqslant N_D$, electrons tunneling through the potential barrier;

(2) Thermionic emission (TE): when $N_D \leqslant 10^{17}$ cm^{-3}, electrons emit over the potential barrier;

(3) Thermionic field emission (TFE): when 10^{17} $cm^{-3} < N_D < 10^{19}$ cm^{-3}, electrons thermally tunnel through the potential barrier.
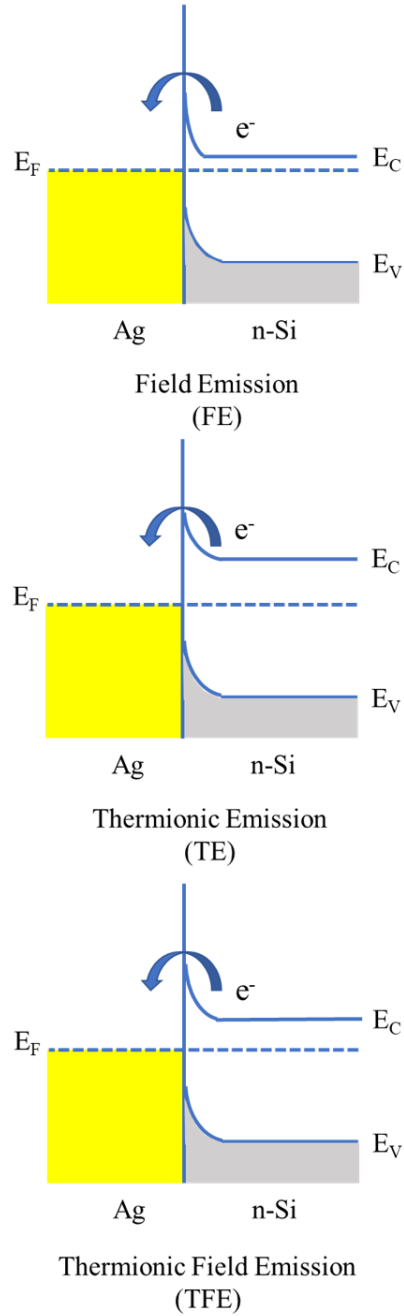
Figure 1.9: Current flow mechanisms of the metal semiconductor contact.

The specific contact resistance ρ_c is defined as

$$\rho_c = \left(\frac{\partial J}{\partial V}\right)^{-1}_{V=0} \tag{1.6}$$

where J is the current density of a metal-semiconductor contact and V is the applied voltage.

In the FE region, when $10^{19} \ cm^{-3} \leq N_D$ [8],

$$\rho_{c,FE} = \left(\frac{A\pi q}{kTsin(\pi c_1 kT)} \cdot exp\left(\frac{-\phi_B}{E_{00}}\right) - \frac{Ac_1 q}{(c_1 kT)^2} \cdot exp\left(\frac{-\phi_B}{E_{00}} - c_1 u_F\right) \right)^{-1} \quad (1.7)$$

where

$$A = \frac{4\pi m^* q(kT)^2}{h^3} \quad (1.8)$$

$$E_{00} = \frac{q\hbar}{2}\sqrt{\frac{N_D}{m^*\epsilon}} \quad (1.9)$$

and if $\phi_B \gg u_F$,

$$c_1 = \frac{1}{2E_{00}} \cdot ln\left(\frac{4\phi_B}{u_F}\right) \quad (1.10)$$

And the Equation 1.7 is valid if

$$1 - c_1 kT > kT(2E_{00}u_F)^{-\frac{1}{2}} \quad (1.11)$$

where q is the electronic charge, $\hbar$ is Planck's constant divided by 2π, N_D is the doping concentration, m^* is the effective mass of the tunneling electron, ϵ is the dielectric constant of the semiconductor, k is Boltzmann constant, T is the temperature, ϕ_B is the barrier height, u_F is the Fermi energy with respect to the energy band edge in the semiconductor bulk.

In the thermionic field emission (TFE) range, when $10^{17} \ cm^{-3} < ND < 10^{19} \ cm^{-3}$

$$\rho_{c,TFE} = \left(\frac{kT}{qA}\right) \cdot \frac{kT}{\sqrt{\pi(\phi_B + u_F)E_{00}}} \times cosh\left(\frac{E_{00}}{kT}\right)\sqrt{coth\left(\frac{E_{00}}{kT}\right)} \times exp\left(\frac{\phi_B + u_F}{E_0} - \frac{u_F}{kT}\right)$$
$$(1.12)$$

where E_0 is a measure of tunneling probability in the TFE region,

$$E_0 = E_{00}coth\left(\frac{E_{00}}{kT}\right) \quad (1.13)$$

And Equation 1.12 is valid if

$$\frac{cosh^2\left(\dfrac{E_{00}}{kT}\right)}{sinh^3\left(\dfrac{E_{00}}{kT}\right)} < \frac{2(\phi_B + u_F)}{3E_{00}} \quad (1.14)$$

In the thermionic emission (TE) range, when $N_D \leq 10^{17} \ cm^{-3}$,

$$\rho_{c,TE} = \frac{kT}{qA}exp\left(\frac{\phi_B}{kT}\right) \quad (1.15)$$

Thus, ρ_c is proportional to $exp(\frac{\phi_B}{\sqrt{N_D}})$ and the trend of ρ_c with decreasing the N_D

is shown in Figure 1.10.
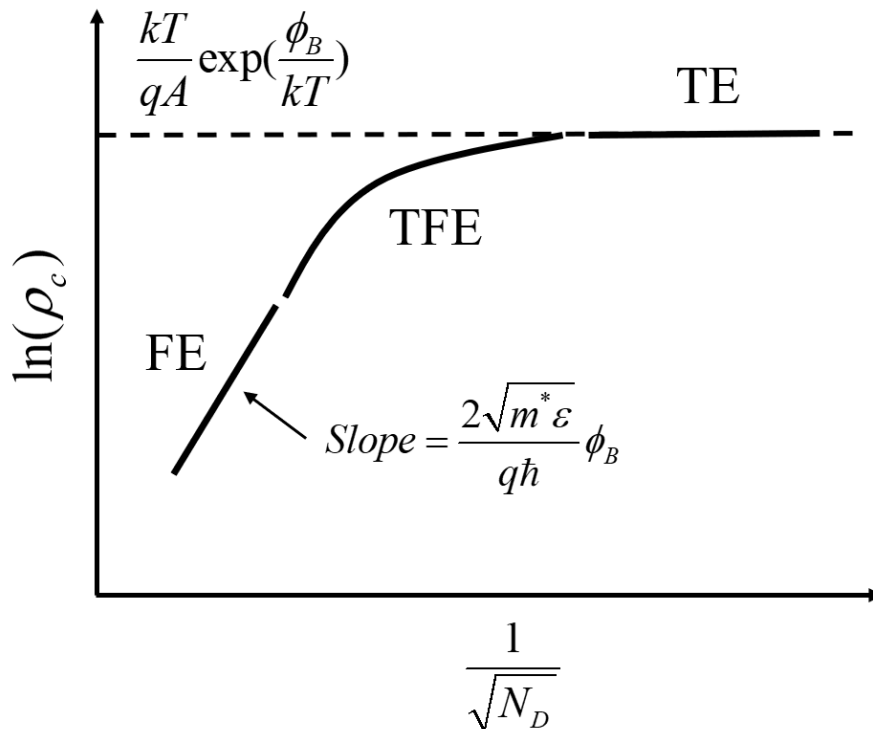
Figure 1.10: Theoretical dependence of the specific contact resistance on the doping concentration.

Based on the PC1D modeling, the 140 Ω/sq emitter has surface doping concentration of 4.4×10^{19} cm^{-3} and the commercial 90 Ω/sq emitter has that of 7.9×10^{19} cm^{-3}. Thus, according to Equation 1.7, 140 Ω/sq emitter will have ρ_c of 5.21×10^{-4} Ωcm^2 which is $\sim$ 24 times larger than that of 90 Ω/sq emitter of 2.13×10^{-5} Ωcm^2. As shown in Figure 1.11, for 1.0×10^{19} $cm^{-3} < N_D < 1.0 \times 10^{20}$ cm^{-3}, ρ_c decreases with increasing N_D.
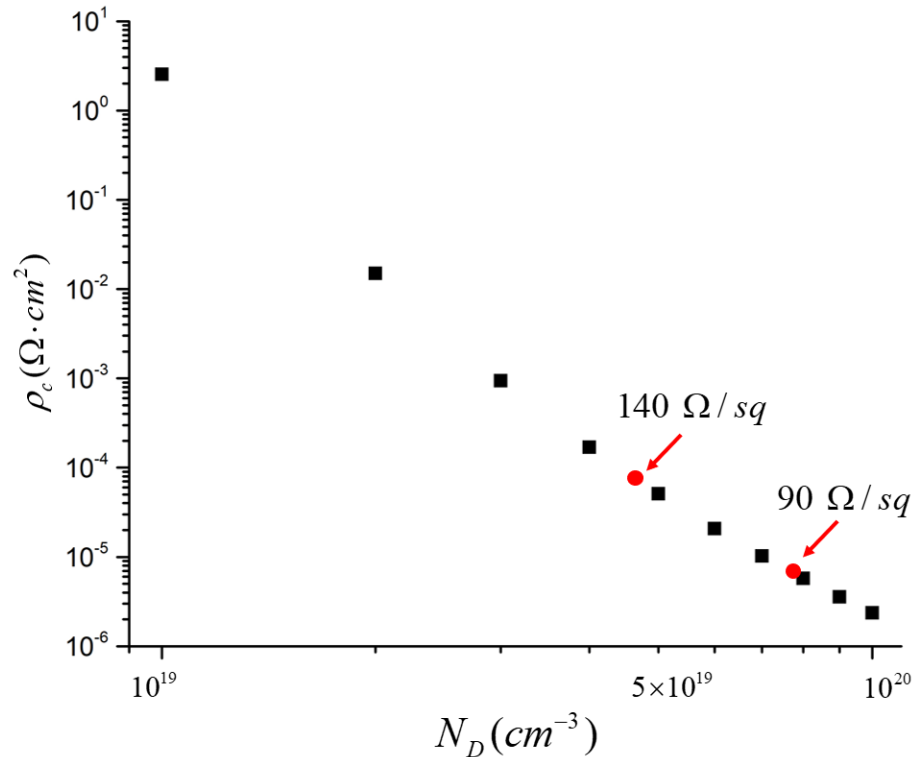
Figure 1.11:   The change of specific contact resistance with increasing doping concentration.

Thus, to achieve higher efficiency though application of the lowly doped emitter in conjunction with the fine gridlines to reduce the cost with either Ag, Ag-Cu or Cu paste, the specific contact resistance must be as low as possible. Because of this, it is important to understand the contact mechanisms of Ag/Si contact in screen printed Si solar cells before the fabrication of narrow Ag contacts or Ag-Cu or Cu contacts.

1.4.2   Contact Mechanisms in the Ag/Si Contact

The front metallization in the Si solar cell is manufactured by firing the screen-printed Ag contacts under peak high temperature for a short time as described in section 1.2.2. Based on the microstructure of the Ag/Si contact, there are four current transport paths, as shown in Figure 1.12.

(1) through Ag fingers direct contact with Si emitter;

(2) through Ag crystallites direct contact with Si emitter;

(3) tunneling through an ultrathin glass layer;

(4) through Ag nanoparticle assisted tunneling;
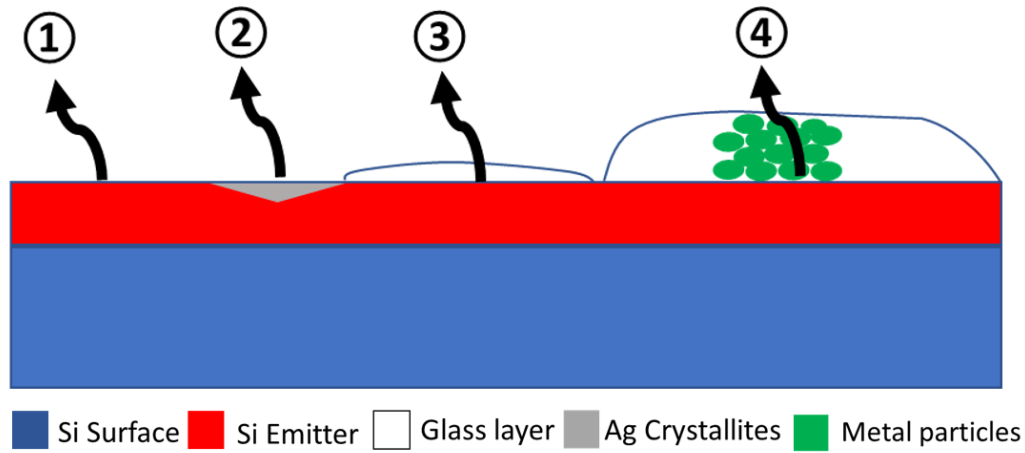
Figure 1.12: Schematic drawing of current transport paths in the Ag/Si contact.

Path (1) is the ideal current transport path where Ag fingers directly contact with exposed Si emitter without extra etching. The specific contact resistance of path (1) can be calculated according to the pure metal-semiconductor contact as discussed in section 1.4.1 based on the surface doping concentration. But the direct contact area, compared with the whole surface area, is small and only occurred on the top surface of the Si pyramids [7].

Compared with path (1), next desired path is through Ag crystallites, path (2), which can also be treated as pure metal-semiconductor contact. But, the formation of Ag crystallites is because of the Ag ions in the glass further etching of Si emitter [9], which is dependent on both the paste properties and the firing conditions [10, 11, 12, 13]. The specific contact resistance for Ag crystallites does not sit right on the top of the emitter top surface doping concentration and is impacted by the etching depth, because the dopant concentration of phosphorus emitter decreases dramatically with increasing in depth from the surface [14]. In this case, the deep growth of Ag crystallites will result in higher specific contact resistance [15]. In addition, as the doping concentration reduces, the p-n junction will be shallower [14]. Hence, Ag

crystallites are not desired for the lowly doped emitter because of the higher risk of penetrating the p-n junction.

Paths (3) and (4) are the least effective contact paths because both are highly dependent on the properties of the interface glass layer (IGL), especially its thickness and the embed metal nanoparticles. For carrier conduction through a pure insulator glass layer (SiO_2), the glass thickness has to be less than 3.6 nm and the specific contact resistivity can be calculated based on a semi-empirical tunneling current model [16, 17]. When the glass thickness is thicker but less than 20 nm, conduction can still transpire, but only if there are sufficient metal nanoparticles embedded in it [17]. However, controlling the IGL thickness to be thinner than 20 nm is challenging because it requires specific amount of glass frits to completely and uniformly etch through the ARC.

Because completely etching through the ARC requires a tailored amount of glass frits in the Ag paste, the IGL normally is thicker than 20 nm and uniform as well. In order to achieve low specific contact resistance at the same time, such thick glass must be conductive.

1.4.3   Challenges for Cu Pastes

The understanding of the Ag fire through contacts can be extended to the Ag-Cu or Cu fire through contacts. However, the main problem that hinders the application of Cu in Si solar cells is the fast diffusion of Cu into Si during the firing. The diffused Cu ions create carrier recombination sites [18, 19], cause copper related light-induced degradation (Cu-LID) of the minority carrier lifetime [20] and form Cu3Si compound which can shunt the p-n junction [21]. Compared with the Cu oxidation problem, preventing Cu from diffusing into Si is the primary requirement for Cu metallization in Si solar cells. Thus, a diffusion barrier is essential to be formed between Si bulk and Cu contacts. But fabricating the diffusion barrier requires other techniques, such as plating [22, 23, 24] and depositing [25], along with photolithography based

wet chemical etching and laser ablation to open the ARC. Although the fabricated diffusion barrier enables the device work properly, the whole metallization process step is expensive and far from commercialization. Since FTDC is the most cost-effective process for front metallization in Si solar cells, using FTDC process to fabricate the Ag-Cu or Cu front contacts will be the best choice. However, the major uphill in this process is to formulate a Ag-Cu or Cu paste with appropriate conductive glass that will prevent the Cu from diffusing into the Si under high temperature and lower the contact resistance.

1.5   Research Objectives

This thesis work investigates the current transport mechanism at the Si/gridline interface of the screen-printed commercial silicon (Si) solar cell with lightly doped emitter. The use of lightly doped emitter is one way to improve the efficiency of the Si solar cell without any additional cost. Another way to decrease the cost of solar electricity is to replace the Ag used for the front gridline with a screen-printable Ag-Cu or Cu pastes. Thus, the objective of this work is to characterize the Ag/Si interface to elucidate the current transport and then extend to Ag-Cu/Si interface, which are formed with screen-printable pastes consisting Ag powder (and or Cu at some wt%), glass frits and organic binders. For screen-printable contacts formed on heavily doped emitter, the contact resistance at the Ag/Si is always low but because of the shadowing and surface recombination losses, the cell efficiency is low. In this work, the Ag/Si interface on lightly doped emitter was first studied to elucidate the understanding of the transport mechanisms at the interface and then the Ag-Cu/Si interface.

This dissertation is composed of five chapters including; introduction in chapter 1, three articles in chapters 2 to 4, and chapter 5, the conclusion:

1.6   Dissertation Outline

Chapter 1: Introduction

Chapter 2: The Role of Nano-crystallites on Conduction Mechanisms of Current Through Ag Gridlines of Si Solar Cells (published in MRS Advances, 2018)

Chapter 3: The impact of Semimetal Nanoparticles in the Thick Glass Layer at the Ag/Si Interface of the Fire through Dielectric Contact on Si Solar Cells (under review - Journal of Colloid and Interface Science)

Chapter 4: Investigation of the Screen-printable Ag-Cu Contact for Si Solar Cells Using Microstructural, Optical and Electrical Analyses (published in MRS Advances, 2019)

Chapter 5: Conclusions

CHAPTER 2: The Role of Nano-crystallites on Conduction Mechanisms of Current Through Ag Gridlines of Si Solar Cells

2.1 Abstract

In order to understand the impact of nano-crystallites on current transport mechanisms in screen-printed c-Si solar cells with lowly-doped emitter, Te-glass based Ag pastes with different transition temperatures (T_g) were used. The Te-glass with lower T_g showed lower Rc than the one with higher T_g due to the formation of nano-crystallites in the glass layer. These nano-crystallites enhance the conductivity of the glass and lead to higher fill factor (FF). The nature of these nano-crystallites was first identified by the Raman spectrometry and the peaks at 76 cm^{-1}, 119 cm^{-1} and 145 cm^{-1} were corresponding to Ag_2Te and PbTe. The conductive-AFM further confirmed the high conductivity of these nano-crystallites without pyramidal Ag crystallites, which means the current transporting from Si emitter to Ag gridlines is mainly through the nano-crystallites in the glass.

2.2 Introduction

For solar electricity to reach $0.03 kW/h in 2030 as predicted by the Department of Energy (DOE) [26], the efficiency of solar cells must approach the material limit. For instance, Si which holds the largest market share in solar industries, its theoretical efficiency can be $\sim 30\%$ [27]. However, since the efficiency is a product of the open circuit voltage (V_{oc}), short circuit current density (J_{sc}) and FF, these parameters must be increased simultaneously. In a study by ITRPV [28], the lowly-doped emitter with sheet resistance $\sim 140\ \Omega/sq$ is the target to achieve high efficiency by enhancing both V_{oc} and J_{sc}, because the lowly-doped emitter is more transparent to photons. But it is

hard to contact such emitter with high $FF > 82\%$ and it requires a new understanding of the screen-printed contacts on the lowly-doped emitter ($\sim 140 \ \Omega/sq$).

To achieve high FF, the total series resistance (Rs) encompassing emitter, gridline, busbar, bulk, back and contact (Si/Ag-gridline) should be very low. Technically, the emitter resistance is addressed by decreasing the finger spacing; gridline resistance is reduced by improving the paste rheology to fabricate continuous and thick gridlines plus increasing the number of busbars; busbar resistance is decreased by increasing the weight percent ($wt.\%$) of Ag solids in the paste and avoiding line breakage; bulk resistance is fixed and the resistivity normally is $\sim 2 \ \Omega - cm$ to reduce the light; back resistance is lowered by having uniform Al alloying in the $\sim 10\%$ back contact area and for the aluminium back surface field (Al-BSF) solar cells, uniform BSF is important. This leaves the front contact resistance (Si/Ag-gridline), which is said to depend on the emitter peak surface concentration. The highest FF reported today on screen-printed solar cells, for example, Al-BSF cell is 80.92% [29] and that of the passivated emitter and rear cell (PERC) is 81.49% [30]. In this work, the role of nano-crystallites formed in the glass on current conduction between Si and gridlines is assessed. The formation of such nano-crystallites in the glass is seen to reduce the contact resistance and lead to high FF.

2.3   Theory

2.3.1   Contact Resistance and Current Transport Mechanisms at the Si/Ag-gridline Contacts

According to Goetzberger [31], contact resistance (Rc) is given as

$$R_c = \frac{\rho_c}{l \times L} \tag{2.1}$$

where l is the length and L is the width of the gridline and ρ_c is specific contact resistance given by [32]

$$\rho_c = \frac{k}{qTA^*} \cdot exp(\frac{4\pi\sqrt{\epsilon_{Si}m^*}}{h} \cdot \frac{\Phi_{Bn}}{\sqrt{N_s}}) \tag{2.2}$$

where k is the Boltzmann constant, q is the elementary charge, T is the temperature in K, A^* is the effective Richardson constant, ϵ_{Si} is the permittivity of Si, m^* is the effective mass of the charge carriers, h is the Planck constant, Φ_{Bn} is the metal-semiconductor barrier height and N_s is the surface doping concentration.

From equation 2.1, the geometry (l and L) of the gridline has an impact on Rc and could be optimized by changing the number of busbars (BB) [33] and narrowing the gridline separation [34]. Eventually, Rc is dependent on ρ_c. According to equation 2.2, lowly-doped emitter has higher ρ_c due to low N_s and hence higher Rc. In addition, for the screen-printed technology, the Ag gridlines are contacting not right on the top of Si surface, but several nanometers underneath it. It was found that the concentration of phosphorus decreased dramatically as the depth and it showed from the top surface to below $33nm$, the N_s decreased from $5 \times 10^{20}\ cm^{-3}$ to $1 \times 10^{20}\ cm^{-3}$ [35]. Moreover, the contact between Ag gridlines and Si emitter is not pure metal-semiconductor contact. It has a thin glass layer and metal crystallites at the interface [11]. The effect of the thin glass layer and the Ag crystallites on the current transport mechanisms is unclear. One well-accepted hypothesis is that the major current flow into the Ag gridlines is through the pyramidal Ag crystallites which directly contact with bulk Ag. This hypothesis was supported by conductive-AFM [36], microscopic I-V measurement [37] and theoretically calculation [38]. However, some researchers found that the pyramidal Ag crystallites were not necessary for a low Rc and high efficiency was achieved without pyramidal Ag crystallites [39]. In addition, the electron tunnelling assisted by nano-Ag colloids in the interface glass played a more important role in current transport mechanisms than the Ag crystallites. The more Ag colloids in the glass layer, the lower the Rc [40].

To understand the current transport mechanisms in the solar cell front contacts and reduce Rc, one main method is to modify the Ag paste constituents, which contain metal powder ($\sim 85\%$), glass frits ($\sim 5\%$), organic binder ($\sim 10\%$) and additives

such as phosphorus dopant (PV168), Al, Cu etc. The addition of phosphorus dopant
[41] did not yield any useful results because of the longer time it required for the
phosphorus doping to the contact region, the higher firing temperature ($\geq 835\ ^oC$)
and forming gas annealing [42]. In addition, the Al additives needed to be fired under
optimized temperature to avoid forming Al-Si alloy and shunting the p-n junction
[43]. Furthermore, the Cu additive led to the formation of CuO_x during the firing
and requires forming gas annealing [44].

The alternative way to modify paste is using the glass frits with different transition
temperatures (T_g) and crystallization behaviours [11, 45]. By changing the ratio of
TeO_2/ZnO [46], TeO_2/PbO [47, 48], and TeO_2/Bi_2O_3 [49], the T_g of glass frits were
changed. It was found that during the contact formation process, the glass frits with
too low T_g started to flow earlier during the firing. There were two results: (1) the
glass frits had earlier fluidization to etch the anti-reflection coating (ARC) and an
earlier dissolution of Ag particles [11]. As a result, large Ag-crystallite precipitates
were formed to penetrate the junction. (2) The glass frits would soften and flow
more easily to form a thicker glass layer, which prevented photoelectrons from being
collected. For high T_g glass frits, they needed higher sintering temperature and had
insufficient time to wet the Si surface, which caused an incomplete etching of ARC
and had gaps between gridlines and emitter. Thus, the FF was low [48]. However,
the function of TeO_2 in glass frits is not completely understood and the formation
of Ag$_2$Te and PbTe after contact formation process have not been studied. In this
paper, (1) Raman Spectrometer, (2) conductive-AFM, (3) SEM, and (4) EDS analyses
have been used to elucidate the formation of Ag$_2$Te and PbTe, which are believed to
decrease the Rc for lowly-doped emitter.

2.4   Experiment

The p-type Czocralski wafers with bulk resistivity of $\sim 2.5\ \Omega - cm$ were textured
and followed by phosphorus diffusion at 890 ^oC to form 95 Ω/sq emitter. After

that, the wafer edges were isolated and the phosphorus glass was removed followed by PECVD SiN$_x$ (73 nm) deposition. The wafers were divided into four groups for four Ag pastes (A, B, C, D) based on TeO_2 glass with different T_g. Three-busbar structure for full Al-BSF was used in this experiment. The four front Ag pastes were screen-printed in turn onto the wafers with back Al contact already printed and dried. After drying the front Ag paste, the cells were co-fired in the rapid thermal processing (RTP) infrared belt furnace at 230 inch per minute (ipm) at 815 ^oC peak temperature. The fabricated cells were first characterized by light I-V measurements, then one cell from each group was cut into 2 mm strip and the contact resistance was measured.

To investigate the contact interface between the underlying Si and gridline, the cut samples were generated into three sets, (a) as fired (AF); (b) Ag metal removed by HNO$_3$ but the glass remained (HNO$_3$); and (c) the remained glass removed by HF (HF). However, from the contact resistance measurements, the contact resistance for pastes B to D were similar, therefore, other analyses were carried out on samples only with pastes A and D, with highest and lowest Rc and Rs. The microstructure, elemental composition and conductive properties of these samples were evaluated with field-emission scanning electron microscope (FESEM) with EDS (FEI Verios 460L), Raman spectrometer (HORIBA, XploRaTMPLUS) excited at 532 nm and conductive-AFM (Asylum MFP-3D).

2.5   Results and Discussion

2.5.1   Chemical Reactions During Contact Co-firing Step

The front Ag contacts are formed by sintering Ag paste under IR belt with temperatures ranging from $400 - 815$ ^oC for a short time. As the temperature increases from low to high, (a) the organic binder burns out; (b) glass frits start to melt and diffuse towards the wafer surface; (c) the melted glass etches away the ARC layer on the wafer surface through the reduction reactions 2.3 and 2.4; after ARC removal,

the glass starts to react with the Si substrate through reactions 2.5 [50] and 2.6 [51]; meanwhile, the formed Pb and Te could further react with Ag and form PbTe and Ag_2Te from reactions 2.7 and 2.8.

$$6PbO_{(in\ glass)} + Si_3N_4 \longrightarrow 6Pb + 3SiO_{2(in\ glass)} + 2N_2 \tag{2.3}$$

$$3TeO_{2(in\ glass)} + Si_3N_4 \longrightarrow 3Te + 3SiO_{2(in\ glass)} + 2N_2 \tag{2.4}$$

$$2PbO_{(in\ glass)} + Si_{(wafer)} \longrightarrow 2Pb + SiO_{2(in\ glass)} \tag{2.5}$$

$$TeO_{2(in\ glass)} + Si_{(wafer)} \longrightarrow Te + SiO_{2(in\ glass)} \tag{2.6}$$

$$Pb_{(s)} + Te_{(s)} \longrightarrow PbTe_{(s)} \tag{2.7}$$

$$2Ag_{(s)} + Te_{(s)} \longrightarrow Ag_2Te_{(s)} \tag{2.8}$$
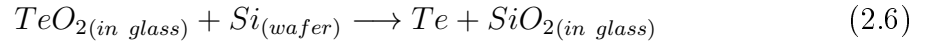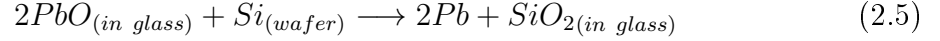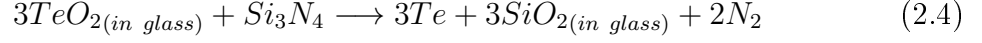
Based on Gibbs free energy, the thermodynamic potential for each possible reaction is shown in Figure 2.1(a) where the potential of reactions 2.7 and 2.8 at 850 ^oC is respectively $-69.54\ kJ/mol$ and $-59.36\ kJ/mol$. It is obvious that for the reactions $2.3 \sim 2.8$, the Gibbs free energy is always negative from 300 ^oC to 850 ^oC, which means each reaction can happen spontaneously.

2.5.2 R_c , R_s and FF of Samples with Four Pastes

Figure 2.1b and 2.1c depict Rc, Rs and the corresponding FF for the four pastes. Paste A shows the highest Rc and Rs with lowest FF. The high Rc for contacts with paste A can be attributed to the thicker glass layer ($\sim 3\ \mu m$) in Figure 2.2a at the interface of Si/Ag-gridline, while the lower Rc for paste D contacts is evident in the thinner glass layer of $\sim 0.7\ \mu m$ in Figure 2.2b.
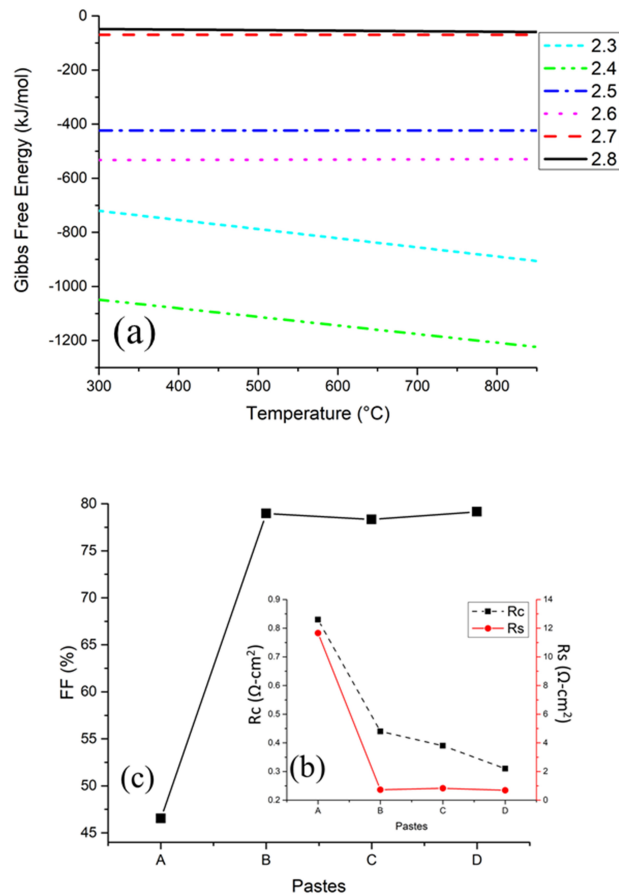
Figure 2.1: (a) Gibbs free energy for possible reactions (1)~(6) under temperature from 300 ^oC to 850 ^oC. (b) Rc and Rs of pastes A-D with (c) FF.

2.5.3   SEM and EDS Analyses

To understand the metal-semiconductor contact interface for the samples with pastes A and D, the microstructure analyse was carried out as shown in Figures 2.2a and 2.2b, respectively. The contact with paste A exhibits a thick non-uniform interface glass layer of $\sim 3~\mu m$ thickness as opposed to those of D with a uniform glass layer of $\sim 0.7~\mu m$ and some Ag nano-particles ($\sim 50~nm$) inside. Figures 2.2c and 2.2d, respectively, show the corresponding EDS for the glass frits in pastes A and D along with the $Pb:Te$ ratio of 3.1 and 1.6 respectively. The $Pb:Te$ ratio is known to impact the T_g of the glass [11, 45]. Since the glass frit in paste A had higher T_g

than that of D, it is possible that higher firing temperature is needed for the glass frits to melt, wet the Si surface, uniformly etch the SiN_x, and then form a thin glass layer with nano-particles inside as in D.
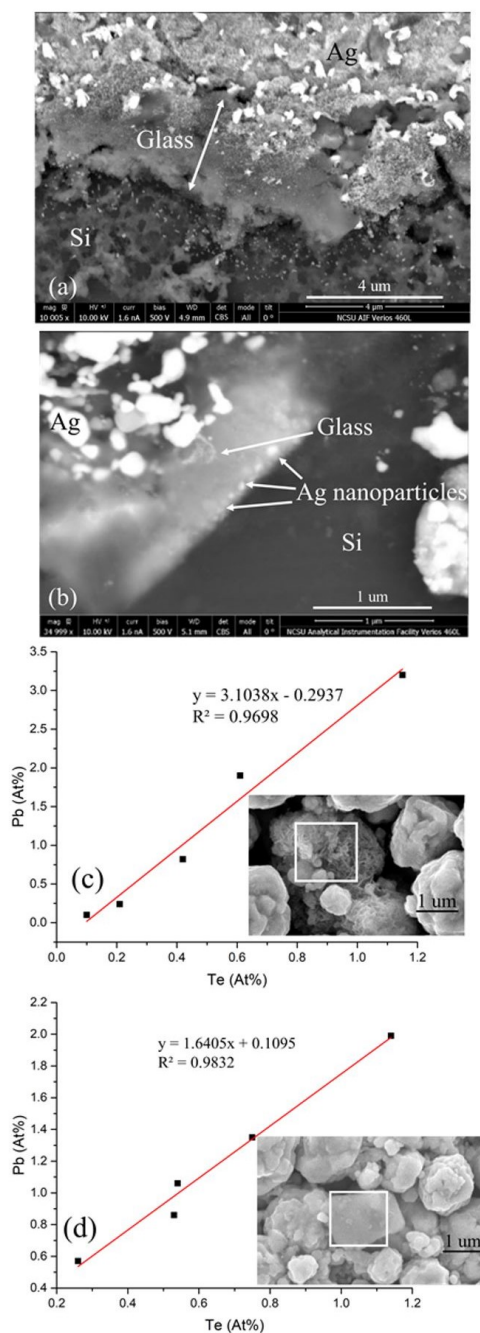
Figure 2.2: (a) SEM images of samples with pastes (a)A and (b)D with $Pb : Te$ ratio of the glass frits in pastes (c) A and (d) D.

Figure 2.3a and 2.3b show the EDS and SEM of the sample with paste A after the Ag gridline was removed with HNO_3. This is an attempt to investigate the location of the nano-particles in the glass, as HNO_3 only removes the Ag gridline without attacking the glass. As seen in Figure 2.3b, there are only few nano-crystallites and the elemental analysis shows no Te in the analysed region. On the contrary, Figure 2.3d for paste D, shows micro-sized bright areas which are large nano-crystallites and such nano-crystallites contain Pb, Ag and Te.

In order to further ascertain the location of these large nano-crystallites, the glass layer was etched off with HF. Because the sample with paste A did not show any crystallites, EDS was carried out only on paste D after HF treatment. As shown in Figure 2.3f, there was few Ag crystallites in the Si for D which indicates the large nano-crystallites were formed right in the glass layer.
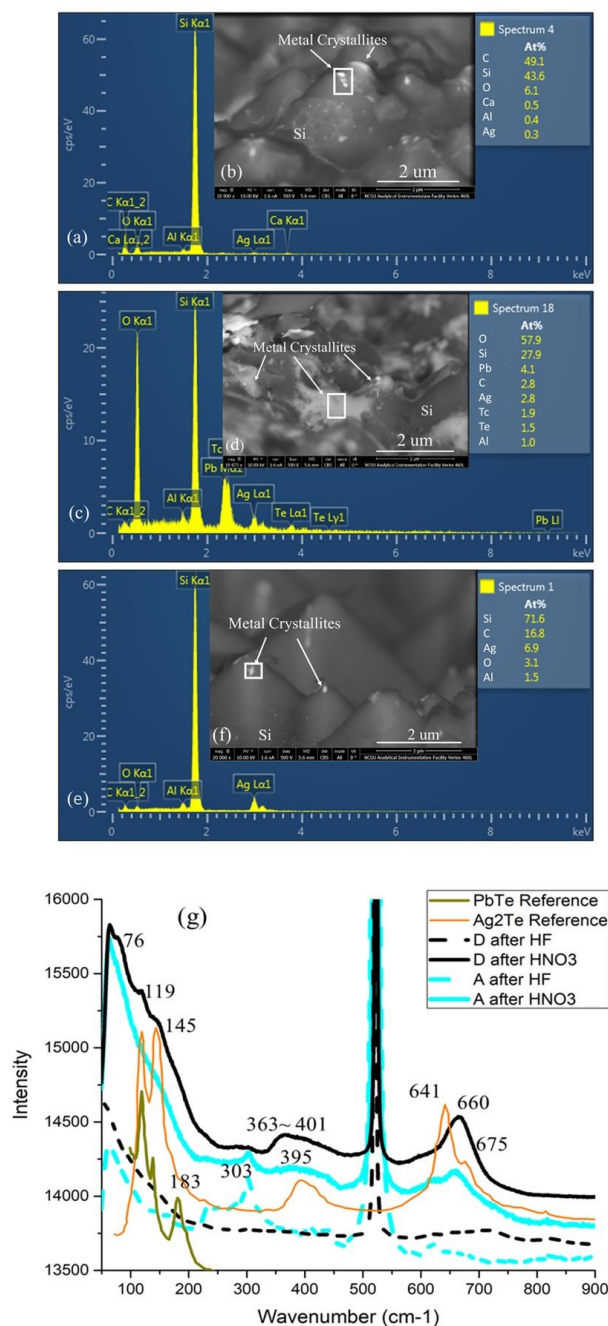
Figure 2.3: EDS elemental analyses of pastes (a) A, (c)D after HNO_3 treatment and (e) D after HF, where the analysed areas are marked by boxes as shown in SEM images: (b) A, (d) D after HNO_3 and (f) D after HF. And Raman spectroscopy (g) of pastes A and D after HNO_3 and HF treatment.

2.5.4   Raman Spectrometer

In order to fully understand the nature of the nano-crystallites formed in the glass layer, the Raman spectroscopy was used. As shown in Figure 2.3 g, after the HNO_3, D exhibits peaks at 76 cm^{-1}, 119 cm^{-1} and 145 cm^{-1} which match the Ag_2Te and PbTe [52, 53, 54]. The peaks around 360-400 cm^{-1} and 660 cm^{-1} are binding vibrations of TeO2 [55]. For A, it only has TeO_2 peaks and no Ag_2Te and PbTe. After the HF treatment, both pastes A and D only show Si peaks at 303 cm^{-1} and 520 cm^{-1}. The Raman spectroscopy confirms that the nano-crystallites formed in the glass for D contains Ag_2Te and PbTe.

2.5.5   Conductive-AFM

In order to understand the distribution of nano-crystallites in the current transport, the glass conductivity was studied by conductive-AFM, where the samples had Ag gridlines removed by HNO_3. The current was measured on the front side after applying a 10V bias on the backside of the sample. In Figure 2.4d, the sample with paste D has micro-sized areas which is very conductive with current over 10 nA, while most area of sample A is non-conducting. The conductive area in D matches the size and shape of the large nano-crystallites in Figure 2.3(d). This suggests that the nano-crystallites in the glass layer enhance the glass conductivity and without these nano-crystallites, the glass is insulator. Thus, the current transports from Si emitter to Ag gridlines mainly through these nano-crystallites of Ag_2Te and PbTe.
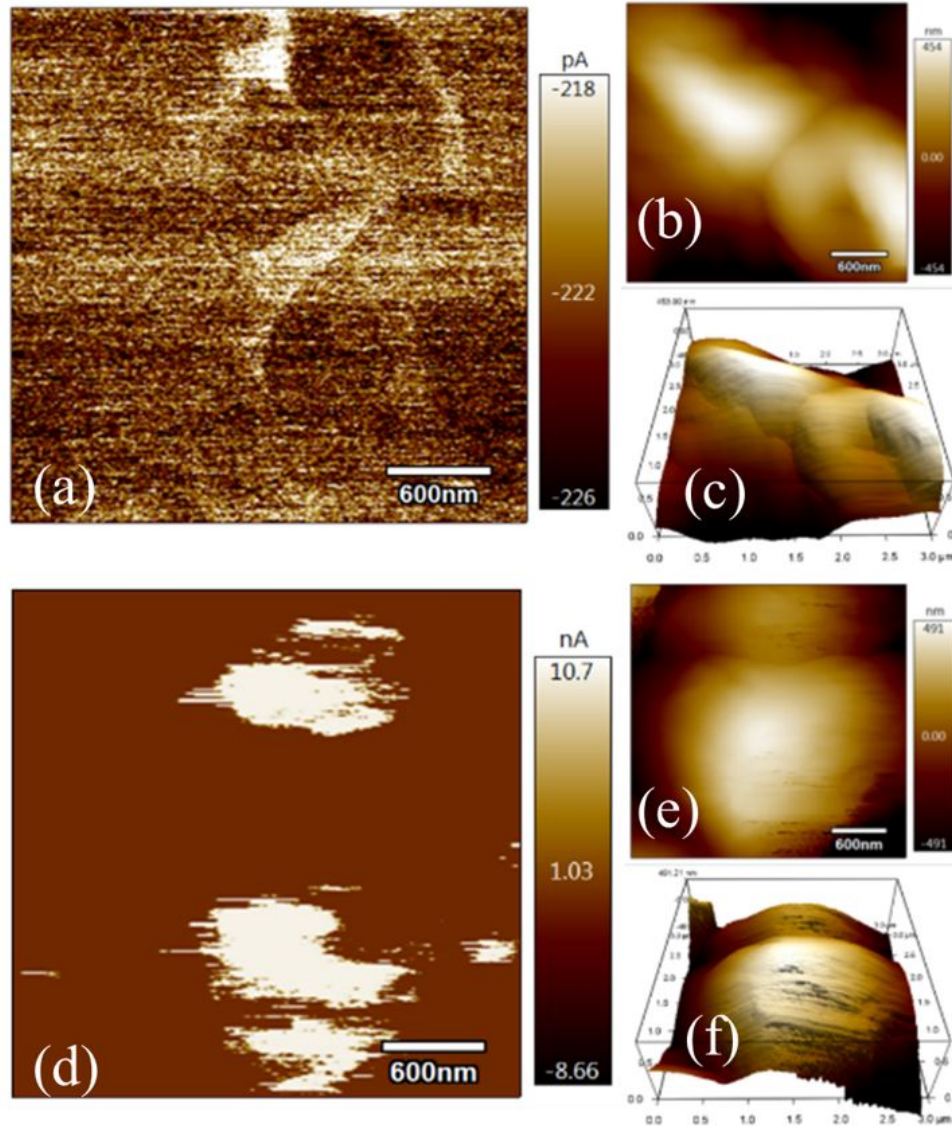
Figure 2.4: Conductive-AFM measurements on samples with pastes A (a~c) and D (d~f) according to current (a & d), height (b & e) and 3D geometry (c & f) measurement.

2.5.6   Conclusion

In this study, it is found that the Pb to Te ratio as well as the T_g of the glass frits can impact the reformed glass at interface of Si/Ag-gridline after contact sintering step. The glass with lower T_g enhances the uniform wetting of the Si surface and SiN_x etching as well as the formation of thinner glass layer with large nano-crystallites. These large nano-crystallites embedded in the glass contain Ag_2Te and $PbTe$ and

increase the glass conductivity. Thus, the current transport from the Si material to Ag gridline is mainly through these nano-crystallites in the glass. In addition, since the pyramidal Ag crystallites were not found in the emitter after the glass layers removal, it suggests that the interface glass plays a more important role in current transport mechanisms than the Ag crystallites.

CHAPTER 3: The Impact of Semimetal Nanoparticles in the Thick Glass Layer at the Ag/Si Interface of the Fire Through Dielectric Contact on Si Solar Cells

3.1 Abstract

This paper reports on the ohmic contact formed on lowly doped emitter through the formation of a conductive bridge which was made up of semimetal nanoparticles embedded in the interface glass layer (IGL) at the Ag/Si interface. The SEM and STEM analyses revealed that the IGL had thickness of greater than $380nm$ and was enriched with micro-sized alloys which were composed of semimetal nanoparticles. This IGL was conductive as confirmed by conductive AFM (c-AFM). The presence of these semimetal nanoparticles, as Ag_2Te and $PbTe$, endowed with low bandgap was confirmed by Raman Spectroscopy and EDS. These semimetal nanoparticles were found only in the IGL and formed a "bridge" to connect the Ag gridline and Si emitter for carrier transport. Based on the modified Fowler-Nordheim tunneling process, the modeled c-AFM I-V characteristic curve showed a barrier height of $0.1eV$ corresponding to IGL thickness of only $18nm$. Thus, the carriers transport through the thick IGL as a bridge formed by the semimetal nanoparticles and the specific contact resistance is independent of the emitter doping concentration.

3.2 Introduction

The high-throughput and low-cost attributes of the screen-printing technology have constrained the front gridlines of the commercial Si solar cells to be formed with the Ag paste. The Ag paste is applied through the screens with narrow openings constituting the gridlines and busbars onto the Si wafer coated with SiN_x antireflective coating (ARC) and then followed by rapid thermal process annealing under high peak

temperature for a short time. During the annealing processes, (i) the glass frits in the Ag paste melt and etch the ARC through redox reaction; (ii) then the molten glass dissolves the Ag metal and further reacts with Si; (iii) after cooling, an interface glass layer (IGL) is formed between the Ag gridline and the Si emitter with Ag particles [56, 39] embedded in the IGL and the Ag crystallites [57] are precipitated in the Si emitter underneath the IGL. The thickness of the IGL depends on the (1) solid Ag particle size [11], (2) the composition of the glass frits [58, 59], (3) the additives [40, 44] in the paste to control the sintering of the Ag particles, and (4) the firing conditions [32, 60].

The IGL thickness has a direct impact on the carrier transport path at the Ag/Si interface. Based on the microstructure of the Ag/Si contact, the carrier transport path from Si emitter to Ag gridline can be characterized into two groups: (1) direct contact with Ag crystallites [32, 36, 37, 38]; and (2) tunneling through an ultrathin glass layer [61] or through Ag nanoparticles assisted tunneling [39, 62]. Thus, thin IGL is preferable for good carrier transport at this interface because it exhibits low contact resistance.

As predicted by ITRPV [28], the lowly doped emitter (140 Ω/sq) is the sure pathway to increase the efficiency of a solar cell due to the decrease in the surface recombination and higher transparency to photons. To achieve ohmic contact on such lowly doped emitter, it requires the understanding of these low contact resistance current transport paths at Ag/Si contact. Among the two groups of carrier paths, through Ag crystallites has been well studied by experimental measurement [32, 37] and theoretical calculations [7, 17]. Under this carrier transport path, the specific contact resistance (ρ_c) of the Ag crystallite contact depends on the emitter surface doping concentration (N_D). Low ρ_c was demonstrated through field emission on heavily doped emitter of $N_D \geq 1 \times 20^{20}\ cm^{-3}$ [8] and as the peak doping concentration decreased, the ρ_c increased rapidly [17]. In this case, contact on the lowly doped

emitter through Ag crystallites will result in much higher ρ_c.

The other carrier transport path is through ultrathin IGL of $1 \sim 3.6$ nm [63], and thicker IGL of $5 \sim 20$ nm with discontinuous Ag nanoparticles [17]. However, realizing uniform IGL of < 20 nm thick is challenging. Hence, in order to achieve ohmic contact on lowly doped emitter, the IGL must be conductive. In addition, this is the preferred carrier transport path that would be independent of the emitter peak surface doping concentration. Thus, it is important to further develop understanding of the formation of the appropriate carrier transport path at the Ag/Si interface for screen printed Ag paste. This work therefore, focuses on developing an understanding of the carrier transport path for lowly doped emitter through microstructure (SEM and STEM and EDS), optical (Raman Spectroscopy) and electrical (c-AFM) analyses. More so, to validate the carrier transport path suggested by these analyses, a modified Fowler-Nordheim tunneling model was applied to model the c-AFM I-V characteristic curves.

3.3   Experimental Methods

The boron-doped p-type 2.5 Ω-cm CZ single-crystalline Si wafers were first cleaned and then texturized followed by POCl$_3$ diffusion to form 95 Ω/sq emitter. After phosphorus glass removal, the ARC SiN$_x$ layer (73 nm) was deposited by PECVD. Then the back Al paste and the front Ag paste were in turn screen printed and dried. After that the Ag and Al contacts were cofired in the rapid thermal processing (RTP) infrared belt furnace at 230 IPM at 815 ^oC peak temperature.

To investigate the microstructure of the Ag gridline/Si contact, the fabricated cell was cut into 2-mm strips and then generated into three sets: (1) with Ag gridline (AG); (2) Ag metal removed by HNO$_3$ with IGL layer remained (HNO$_3$); (3) the IGL layer removed by HF (HF).

The microstructure, elemental composition, electrical property of the sample were evaluated with Field-Emission Scanning Electron Microscope (FESEM) with EDS

(FEI Verios 460L), Scanning Transmission Electron Microscope (STEM) with EDS (FEI Talos F200X), Raman spectrometer (HORIBA, XploRa^{TM}PLUS) excited at 532 nm and conductive-AFM (Asylum MFP-3D).

3.4   Results and Discussion

3.4.1   SEM/EDS and Raman Spectrometer Analyses

Fig.3.1a is the Ag/Si contact interface showing the IGL thickness of > 380 nm. The bright part of the IGL indicates the embedded metal alloys. Fig.3.1b reveals high density of the micro-sized alloys on the emitter that after Ag gridline removal with HNO_3. Fig.3.1c is the EDS elemental analysis, showing the constituent of these alloys, which are mainly Ag, Pb and Te elements. The Raman spectroscopy in Fig.3.1e reveals the formation of Ag_2Te and PbTe semimetal compounds according to the peaks at 76 cm^{-1}, 119 cm^{-1}, 145 cm^{-1} and 183 cm^{-1} [52, 53, 54]. The other peaks at around 390 cm^{-1} and 660 cm^{-1} belong to TeO glass [54]. The redox reactions involved in the formation of both semimetal compounds with thermodynamic potential calculated were reported in our previous work [64]. After HF dip, the SEM image in Fig.3.1d shows the alloys were removed by removing the IGL and it left clean Si pyramids without Ag crystallites. This indicates that semimetal compounds are located in the glass and not in Si. This matches the change in Raman spectroscopy that, after HF treatment, Ag_2Te, PbTe and TeO peaks disappeared. Thus, Ag_2Te and PbTe alloys are encapsulated in the thick IGL and behave as a bridge for carrier transport from Si to Ag gridline.
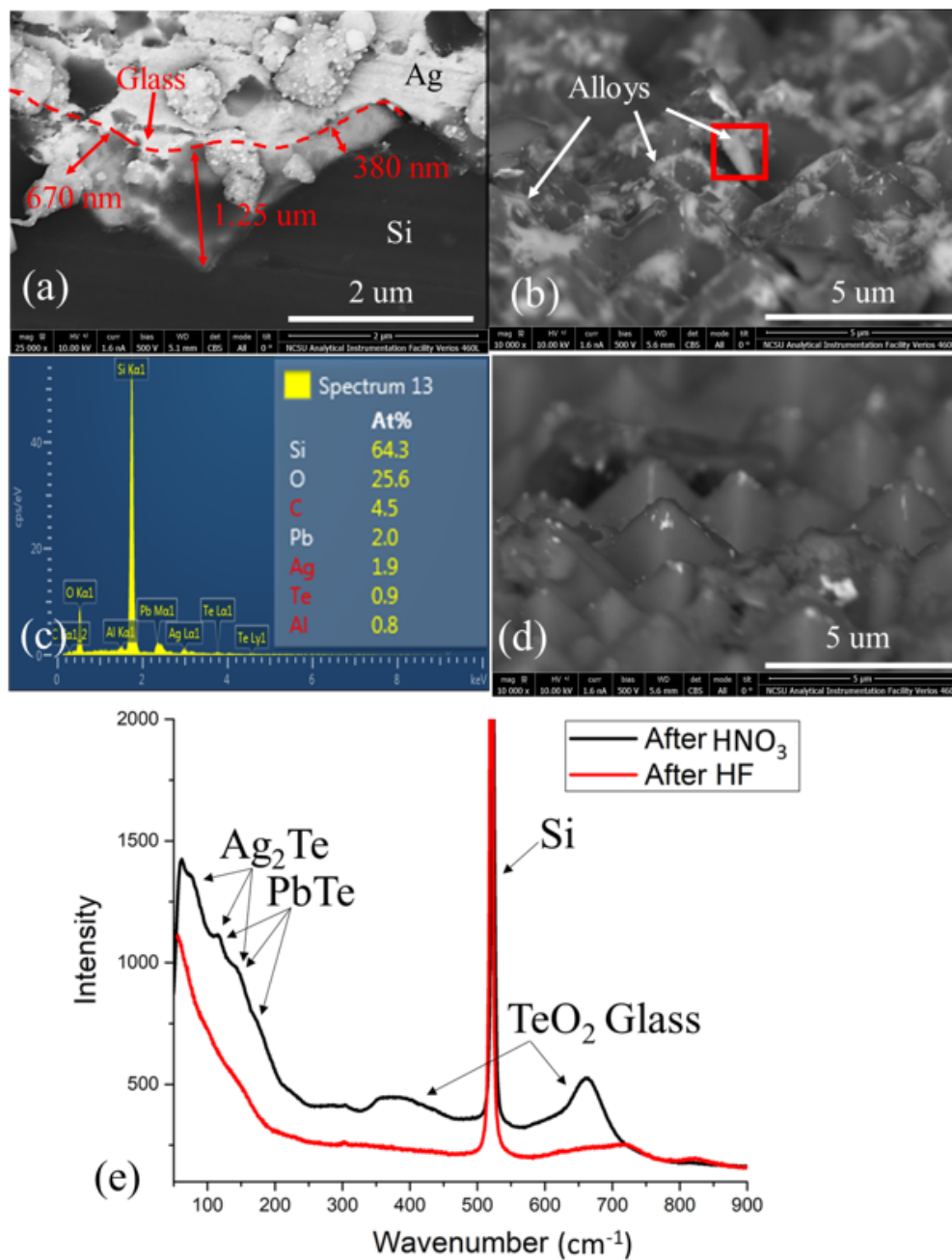
Figure 3.1: SEM images of emitter surface (a) with Ag gridlines, (b) after HNO$_3$ treatment with (c) EDS analysis of the selected area (marked in red box in (b)) and (d) after HF treatment; (e) Raman spectroscopy of the sample after HNO$_3$ and HF treatment.

3.4.2   STEM/EDS Analyses

Further investigating the distribution of the semimetal nanoparticles in the thick IGL was carried out by STEM after the Ag gridlines were removed in HNO_3. Fig.3.2a shows the IGL with a thickness of ~1.3 um, which agrees with the SEM micrograph analysis of Fig.3.1a. Thus, the IGL with thickness of this magnitude will suppress the transportation of carriers to the Ag gridlines. Also, in the IGL, semimetal nanoparticles were embedded, of which the thickness was ~0.9 um with larger percentage of the glass. Figs.3.2b to 3.2e confirm that Ag, Pb, Te are the elements contain in the IGL. Because of the presence of these elements and the peaks shown in the Raman Spectroscopy, these semimetal nanoparticles can be said to be semimetal compounds of Ag_2Te and PbTe. Thus, these semimetal nanoparticles contact the Si emitter and the Ag gridlines and form a conductive bridge, providing a carrier pathway.
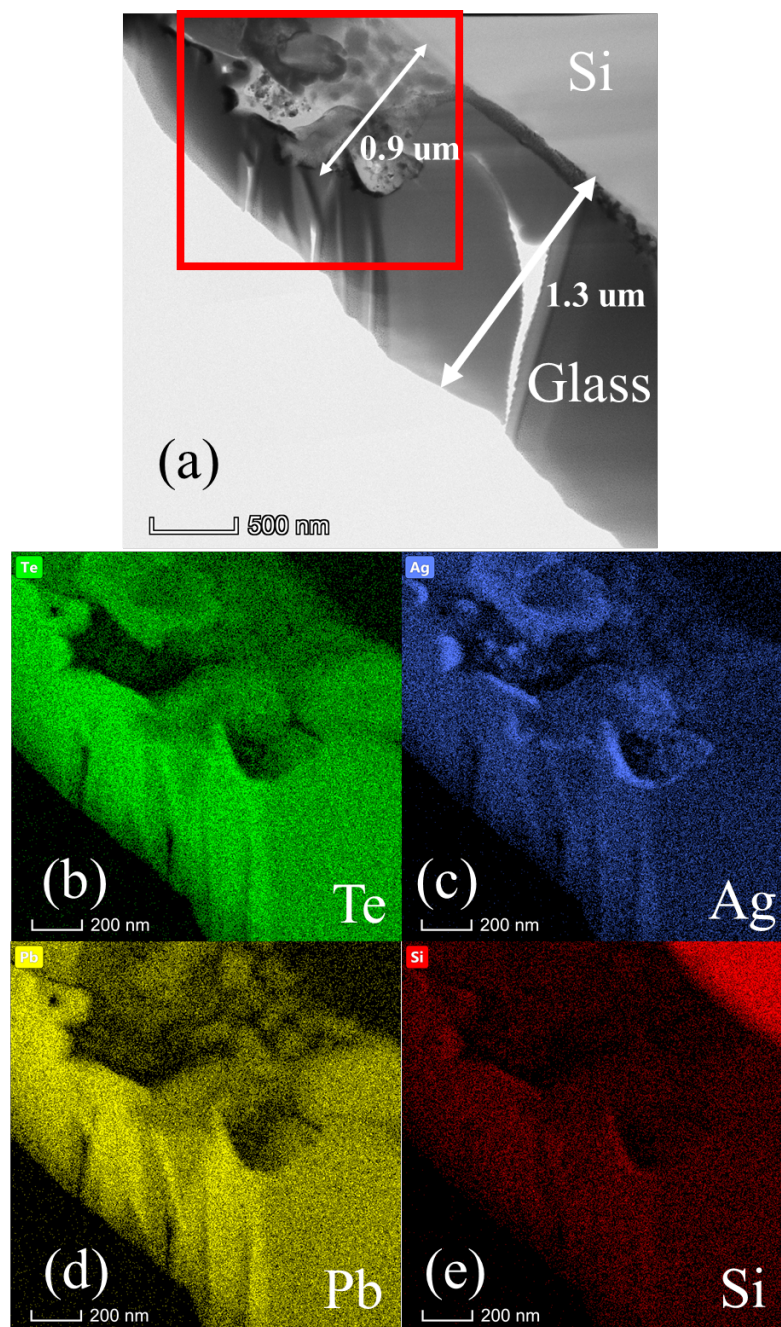
Figure 3.2: (a) STEM image of the glass cross-section and the elemental analysis of selected area (marked in red box) based on (b) Te (green), (c) Ag (blue), (d) Pb (yellow) and (e) Si (red).

3.4.3 Conductive-AFM Analyses

The conductivity of the IGL was mapped by conductive-AFM as shown in Fig.3.3a.

The white micro-sized feature represents the highly conductive area on the IGL with

current larger than 10 nA under $\pm$ 10 V bias. This conductive feature was located on the top of the Si pyramid according to Fig.3.3c. Based on the shape, size and the location, this conductive area matches the alloys found in Fig.3.1b. Through the I-V characteristic curves measured by c-AFM in Fig.3.3d, the ohmic contact was achieved on the alloy region while the rest glass area was nonconductive. The specific contact resistance of the alloy was estimated to be $4.93 \times 10^{-4} \sim 26.94 \times 10^{-4}$ $\Omega \cdot cm^2$ [65], which is comparable to that of Ag crystallites (2×10^{-4} $\Omega \cdot cm^2$) [37]. In this case, the formation of the semimetal nanoparticles in the IGL dramatically increases its conductivity, which forms a conductive path to transport carriers from Si to the Ag gridline. Thus, a new carrier transport path - "through enhanced conductive thick IGL by semimetal nanoparticles" was found.
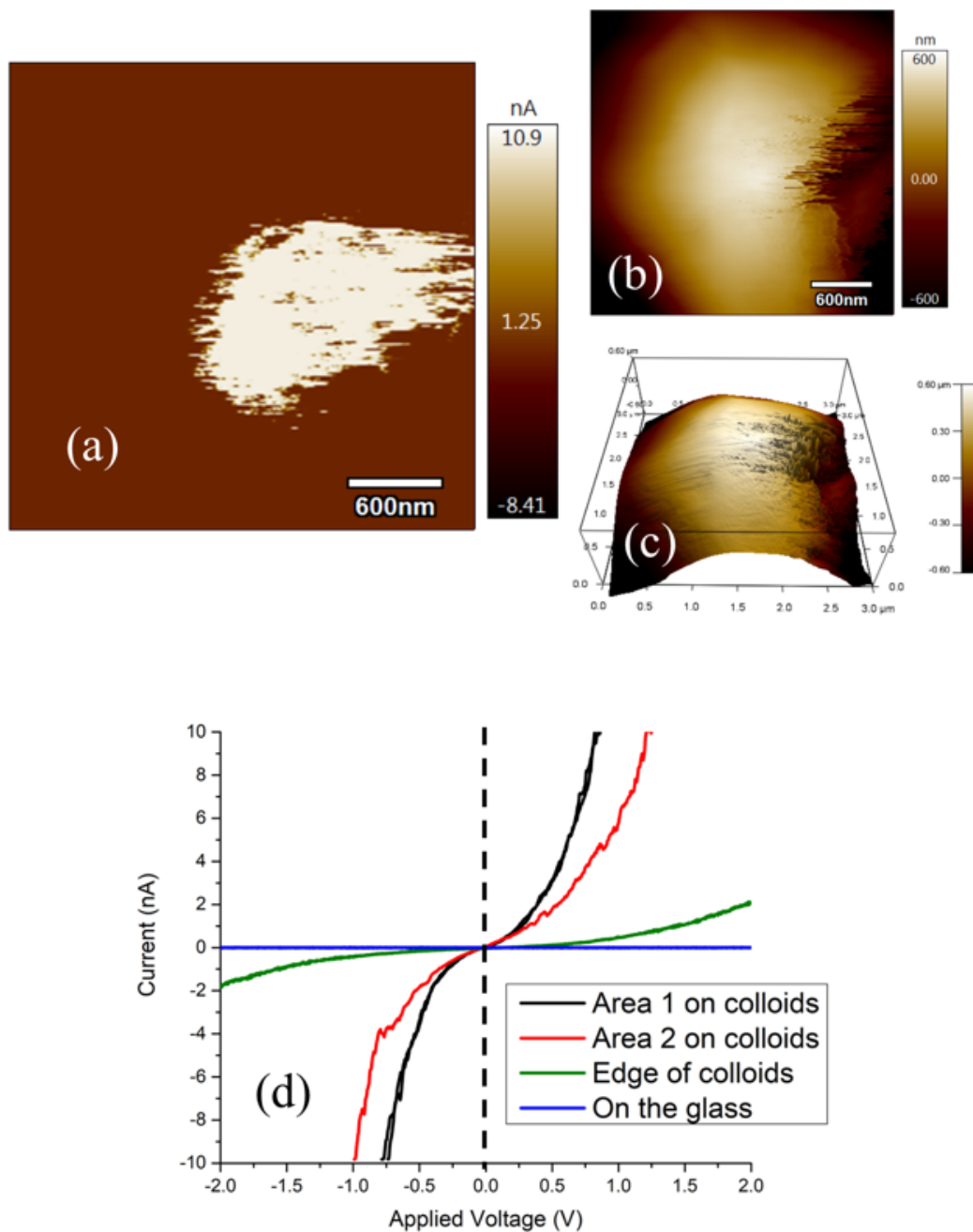
Figure 3.3: Conductive-AFM images of the sample after HNO_3 treatment based on the (a) current, (b) height and (c) 3-D and (d) I-V curves of the conductive areas and the nearby nonconductive area.

3.4.4 Mathematical Model of Semimetal Nanoparticle Assisted Contact

Based on the microstructure observed by SEM and STEM in Fig.3.1b and Fig.3.2a respectively, the schematic view of the semimetal nanoparticles assisted contact is

shown in Fig.3.4a. Instead of carriers tunneling through the IGL, the carriers are conducted through the bridge formed by the embedded semimetal nanoparticles in the IGL.

In order to confirm the carrier transport path by semimetal nanoparticles assisted contact, c-AFM I-V characteristics were modeled according to the modified Fowler-Nordheim tunneling (FNT) [66, 67, 68] given in Equation (3.1).

$$I(V) = \frac{A_{eff}q^3V^2m}{8\pi h\Phi_B d^2 m_0} \cdot exp\Big(\frac{-8\pi\sqrt{2m_0}\Phi_B^{1,5}d}{3hV} \cdot v(V)\Big) \tag{3.1}$$

where

$$v(V) = \frac{0.96V}{\Phi_B} \tag{3.2}$$

$v(V)$ in Equation (3.1) is the correction factor when $V > \Phi_B/q$, A_{eff} is the effective contact area, q is the electron charge, V is the applied voltage, m is the free electron mass, h is the Planck's constant, Φ_B is the barrier height, d is the glass thickness, and m_0 is the effective electron mass.

According to [17]

$$\rho_c = \Big(\frac{\partial J}{\partial V}\Big)_{V=0}^{-1} \tag{3.3}$$

Thus, the

$$\rho_c = \Big(\frac{q^3Vm}{4\pi h\Phi_B d^2 m_0} \cdot exp\Big(\frac{-2.56\pi d\sqrt{2m_0\Phi_B}}{h}\Big)\Big)^{-1} \tag{3.4}$$

Fig.3.4b shows the modeled and measured I-V curves, which are in good agreement. The glass thickness of 17.2~21.5 nm was used in modeling the measured I-V curve, which is much less than the measured glass thickness shown by SEM (>380 nm), in Fig.3.1a. The fact that only ~18 nm thick glass fits the curve, confirms that the semimetal nanoparticles increased the conductivity of the thick IGL, which in turn provided a bridge that the carriers transport through. Moreover, the higher transport current around the center of the conductive area than around the edge suggests that the center of the conductive area had higher density of semimetal nanoparticles.
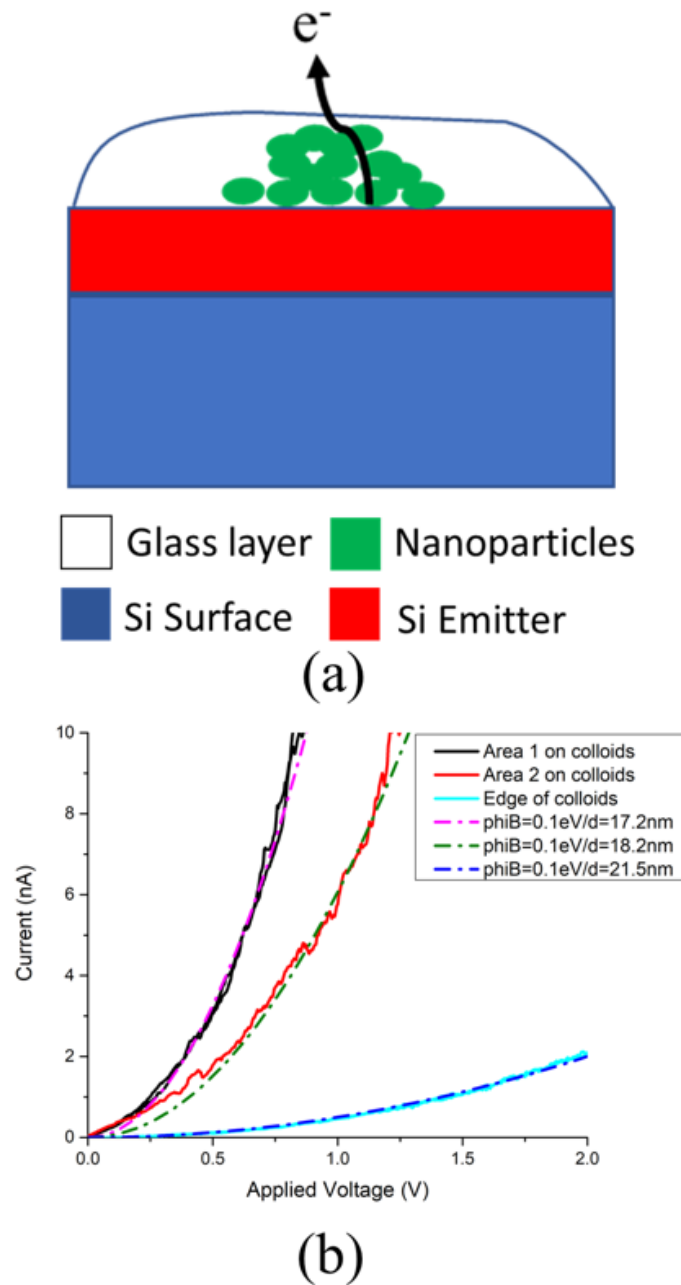
Figure 3.4: (a) Schematic of the Si pyramids (p-Si substrate in blue, emitter layer in red, interface glass layer in white, nanoparticles in green). (b) Measured and calculated I-V curves for the top and edge of the colloid. The modeled barrier height and the glass thickness are indicated.

In addition, in Fig.3.4b, the calculated barrier height for the contact is 0.1 eV, which is much lower than the measured 0.65 eV of the pure Ag/n-type Si (100 Ω/sq)

contact [69]. The low barrier height is attributed to the presence of the PbTe and Ag$_2$Te semimetal nanoparticles. The band gap of PbTe is $\sim$0.30 eV [70, 71], while that of Ag$_2$Te is $\sim$0.014 eV at 300K [72, 73]. Both PbTe and Ag$_2$Te are n-type [74, 75] because of the excess Pb in PbTe and excess Ag in Ag$_2$Te. The work function of PbTe is $\sim$4.30 eV [76], but the work function of Ag$_2$Te has not been fully studied. Based on the photoemission spectrum of Ag$_2$Te [77] and the energy band diagram of Si/PbTe contact [78], and PbTe/Ag$_2$Te contact [79], the energy band diagram of Ag/semimetal nanoparticles (in IGL)/Si contact can be modeled as shown in Fig.3.5. The energy band diagram shows the conduction band alignment between semimetal nanoparticles and Si, and low barrier height between Ag and semimetal nanoparticles. Here, the overall low barrier height (0.1 eV) results from the semimetal nanoparticle "bridge" at the Ag/Si interface. Although the actual contact between semimetal nanoparticles can be more complicated, the barrier height is lowered through semimetal nanoparticles. As a result, the specific contact resistance is independent of the Si doping concentration as shown in Equation (3.4).
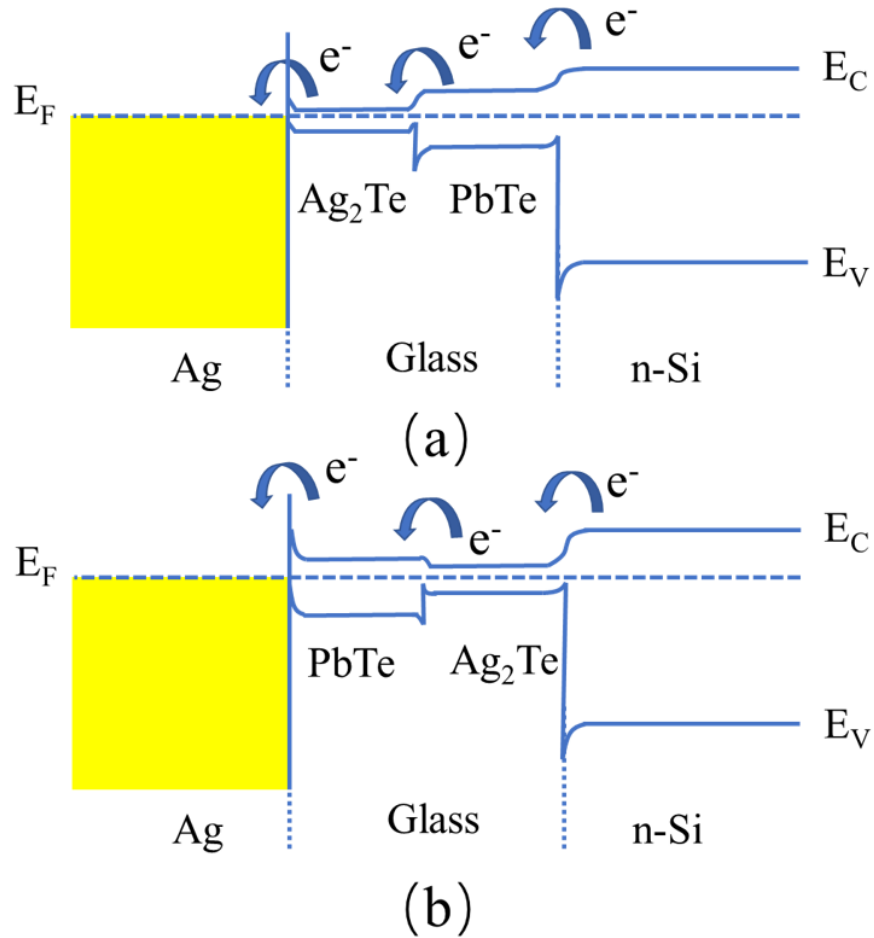
Figure 3.5: Energy band diagram of Ag/ semimetal nanoparticles (in glass)/ Si contact: (a) Ag/Ag$_2$Te/PbTe/Si contact; (b) Ag/PbTe/Ag$_2$Te/Si contact.

Equation (3.1) is used to generate Fig.3.6, which shows the impact of barrier height and IGL thickness on the transport current. When (a) the IGL thickness (d =18 nm) and (b) the barrier height (Φ_B = 0.1 eV) are constant, slight increase in the barrier height and IGL thickness can significantly decrease the transport current. Thus, the presence of Ag$_2$Te and PbTe semimetal nanoparticles in the IGL at high density is very crucial to generate higher transport current.
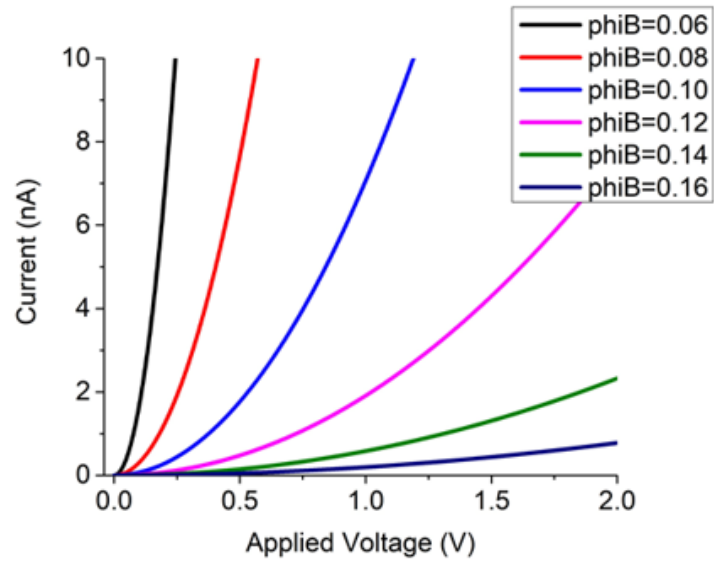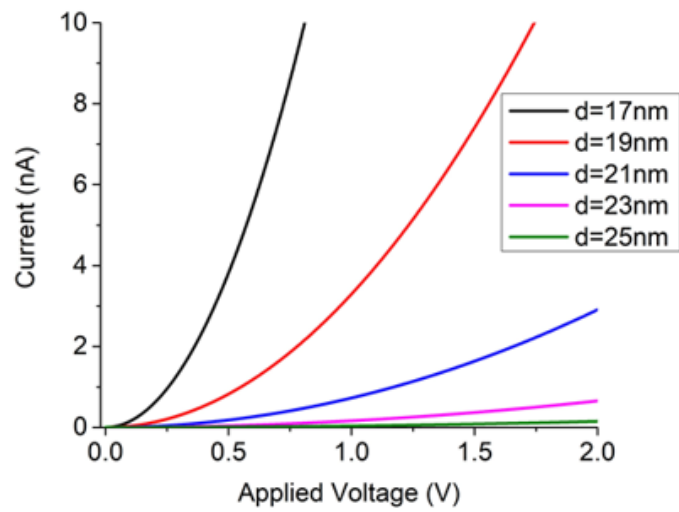
Figure 3.6: Calculated I-V curves of resonant tunneling based on (a) barrier height and (b) glass thickness.

3.5 Conclusion

In this work, the ohmic contact through the thick IGL layer at the Ag/Si interface was studied and established as a new carrier transport path for a lightly doped emitter.

According to the SEM and STEM, an IGL with thickness $\geq$ 380 nm was measured and found to contain a large amount of micro-sized alloys which were composed of semimetal nanoparticles. These semimetal nanoparticles were identified as Ag_2Te and PbTe, which possess low-band gaps. The presence of these low-band-gap compounds, according to the c-AFM measured I-V characteristic curves, led to the high bridge current. Through modeling, based on modified Fowler-Nordheim tunneling process in conjunction with the measured c-AFM I-V characteristic curves, a barrier height of 0.1 eV and IGL thickness of $\sim$18 nm were obtained. This is contrary to the measured IGL thickness, which would result in very high contact resistance under barrier height of 0.65 eV. However, the modeled glass thickness suggests that the presence of high-density semimetal nanoparticles with low bandgap lowered the overall contact barrier height and increased the IGL conductivity, so that the IGL thickness is inconsequential. These semimetal nanoparticles acted as a bridge to transport carriers from Si to Ag. This new carrier transport path is independent of the IGL thickness and the emitter doping concentration, which is critical to achieving ohmic contact on the lowly doped emitter.

CHAPTER 4: Investigation of the Screen-printable Ag-Cu Contact for Si Solar Cells Using Microstructural, Optical and Electrical Analyses

4.1 Abstract

In a bid to further reduce the cost of the front Ag contact metallization in Si solar cells, Cu is the potential alternative to replace the Ag in the Ag paste. However, this requires understanding of the contact mechanism of screen-printable Ag-Cu paste in Si solar cell through rapid thermal process. The pastes with different weight percent of Cu (0 wt%, 25 wt% and 50 wt%) were used and the V_{oc} of the cells was reduced with increasing the weight percent of Cu. This is because the presence of Cu in the paste changed the microstructure of the Ag-Cu/Si contact through Cu doping the glass frits and hence increasing the T_g of the glass. The increased T_g of the glass impeded the uniform spreading of the molten glass and resulted in poor wetting and etching of the SiN$_x$, which lowered ideality factor to less than unity. This also led to the formation of agglomerated Ag crystallites with features of 700 nm in length and 200 nm in depth, which is close to the p-n junction, of which depth is ∼300 nm. However, the interface glass layer acted as an effective diffusion barrier layer to prevent Cu atoms from diffusing into the Si emitter, which is quite remarkable. Furthermore, the conductive AFM revealed the contact mechanism of the Ag-Cu paste was through the Ag crystallites grown in the Si emitter.

4.2 Introduction

The front contact metallization of commercial Si solar cells is dominated by Ag metal due to its high conductivity and chemical stability. However, because of the high cost of Ag metal, metallization is the second most expensive part of solar cell

fabrication after silicon. In order to reduce the cost of the solar cell, the amount of Ag in the screen-printable paste should be replaced with low-cost metal materials. Among all metals, Cu is considered as an alternative because its conductivity of 1.7 $u\Omega$-cm is close to that of Ag , which is 1.6 $u\Omega$-cm, but Cu is about 100 times less costly [80, 81, 82].

The major challenge of using Cu for Si solar cell is the fast diffusion of Cu into the bulk Si at high temperature. The diffusion coefficient of Cu in Si at 500 ^oC can be $2.0 \times 10^{-5} cm^2/s$, which is 15 orders of magnitude higher than that of Al. The diffused Cu atoms in the Si form a defect band close to the middle of the Si bandgap, providing extremely efficient minority carrier recombination sites [83] and resulting in significant Cu-related light-induced degradation (Cu-LID) [84]. Moreover, Cu can react with Si and form Cu_3Si compound with micron-order depth, which can shunt the p-n junction [85]. To avoid Cu diffusion into Si, a diffusion barrier layer of Ni [86, 87], Ti [88], Ti/TiN [89], W [90] has been incorporated into the fabrication of the solar cell. Alternatively, a two-step printing process can be used by separately printing the diffusion barrier layer [91, 92, 93] followed by Cu paste printing or Cu electroplating. The process to fabricate these barriers, especially in the plating, requires extra steps, including photolithography process to mask against plasma etching of the double dielectric layer [86, 87] to open the gridline contacts [89]. More so, extra printing step [91] in two-step printing is needed to print the diffusion barrier before fabricating Cu contacts. Although the devices fabricated through these processes, exhibited acceptable performance, these metallization schemes are expensive and still far away from commercialization. Since screen-printing technology is high-throughput and simple to manufacture solar cells, the most cost-effective method is using the same fabrication process and equipment, but replacing the Ag or part of the Ag in the paste by Cu. In order to implement Ag-Cu or Cu contact, the constituents of the paste must prevent the Cu from diffusing into Si during the high temperature sintering of

the contacts.

In this paper, Cu was added into Ag pastes with different ratios to form Ag-Cu front contacts at one-step atmospherically firing process. The contact mechanism of the Ag-Cu paste was investigated through the microstructural, optical and electrical characterization of the Ag-Cu/Si interface.

4.3   Experiment

Textured p-type Cz Si wafers with bulk resistivity of $\sim$2.5 Ω-cm were doped by phosphorus at 890 ^oC to have the emitter sheet resistance of 95 Ω/sq, followed by the isolation of wafer edges and the removal of phosphorus glass. After that, SiN_x (73 nm) layer was deposited by PECVD. The wafers were divided into three groups for three Ag-Cu pastes (S1, S2, S3) based on the weight percent (wt%) of Cu in the paste, (0 wt%, 25 wt%, 50 wt%, respectively). The full Al-BSF with three-busbar structure was used in this experiment. The three front Ag-Cu pastes were in turn screen-printed onto the wafers with back Al contact already printed and dried. The printed cells were dried under 200 ^oC followed by co-firing in the rapid thermal processing (RTP) infrared belt furnace at 230 IPM under 780 ^oC peak temperature. The fabricated cells were first characterized by Suns-Voc measurements and then one cell from each group was cut into 3 mm strips.

To investigate the contact interface of Ag-Cu/Si contact, the cut samples were generated into four sets, (a) with Ag-Cu metal (Ag-Cu); (b) Ag-Cu metal removed by HNO_3 but the glass remained (HNO_3); (c) the remained glass removed by HF but the Ag crystallites left (HF); (d) The remained Ag crystallites removed by extra HNO_3 treatment (2nd-HNO_3). The microstructure and elemental composition of these samples were evaluated with field-emission scanning electron microscope (FESEM) with EDS (FEI Verios 460L). However, from the saturation current density in the space charge region (J_{02}), S3 didn't have effective contact. Therefore, only S2 was further investigated by conductive-AFM (Asylum MFP-3D) and Scanning Transmis-

sion Electron Microscope (STEM) (FEI Talos F200C) where the STEM sample was prepared by Focused Ion Beam (FIB) (FEI Quanta 3D FEG).

4.4   Results and Discussion

4.4.1   Electrical Output Parameters of the Solar Cells

Table 4.1 lists the electrical characteristics of the solar cells. S1 used the standard commercial Ag paste and exhibited an open circuit voltage (V_{oc}) of 656 mV, ideality-factor (n-factor) of 1.05, J_{02} of 3.0×10^{-9} A/cm^2 and the fitted shunt resistance (R_{sh}) of 77246 Ω-cm^2. This indicates the firing condition (peak temperature of 780 ^oC) is ideal for the commercial Ag pastes. Sample S2, which has 25% Cu, exhibited similar J_{02}, but lower R_{sh}, V_{oc} and n-factor. The ideality factor of less than unity suggests that the peak firing temperature is not appropriate for this Ag-Cu contact, which could either be in the "under firing" or "over firing" state. More work is needed to optimize the peak firing temperature. The fact that the S2 has similar J_{02} as S1 is quite encouraging and suggests that there is no diffusion of Cu into the junction to cause shunting. Sample S3, which used 50% Cu, did not make any contact as suggested by the J_{02} value and R_{sh} with n-factor much less than unity. Therefore, further investigation through optical characterization of the Ag-Cu/Si contact with SEM and EDS was carried out.

Table 4.1: Electrical output parameters of the solar cell with Ag and Ag-Cu fire through dielectric contacts

	V_{oc} (mV)	n-factor	J_{02} (A/cm^2)	Fitted R_{sh} (Ω-cm^2)
S_1	656	1.05	3.0×10^{-9}	77246
S_2	604	0.94	2.9×10^{-9}	63734
S_3	602	0.56	1.0×10^{-11}	150000

4.4.2   SEM and EDS Analyses

Figure 4.1a shows the interface of Ag gridline/Si contact in Sample S1, where the Ag particles were completely melted and mixed during the firing, making the Ag gridline

very uniform. In addition, the thick glass layer, with thickness of 300∼500 nm, was formed right on top of the Si emitter. From the EDS analysis in Figure 4.1b, the glass layer contains Te and Pb elements. After the Ag metal removal in HNO3, in Figure 4.1c, the glass layer completely covered the Si pyramids and according to the EDS, there was no N element left on the surface, which reveals that the thick glass layer ensures complete wetting and etching of the SiN_x during the high temperature firing step. In Figure 4.1e, after the interface glass removal, there are some Ag crystallites formed right on the top of the Si pyramids. The microstructures of the Ag gridline/Si contact in sample S1 matched with the characteristics of the Te-glass based Ag paste [64], while the lower Pb:Te ratio of the glass frits in sample S1 lowered the transition temperature (T_g) of the glass frits and caused more Ag crystallites formation at lower sintering temperature in sample S1.
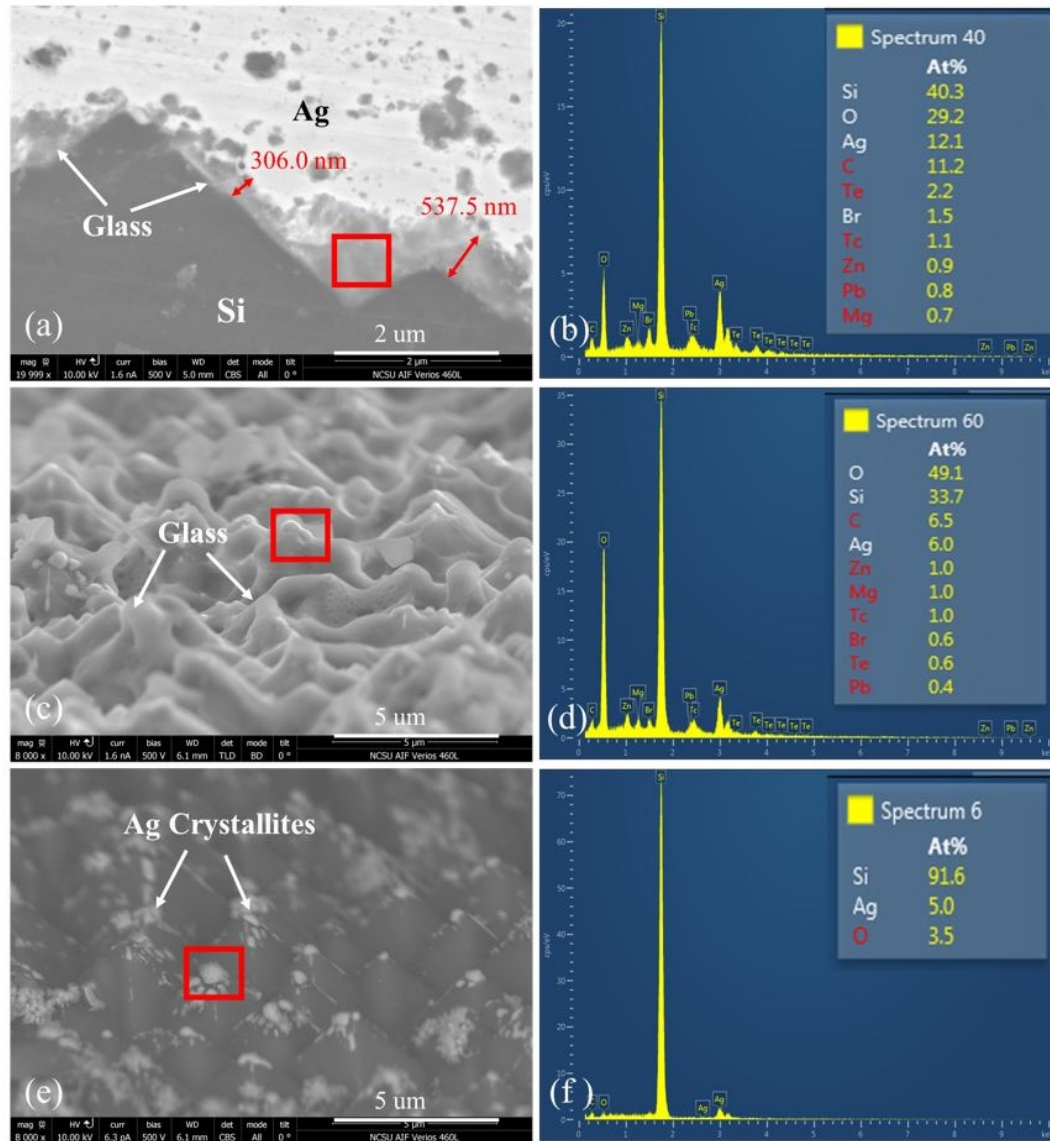
Figure 4.1: SEM images (a, c, e) and EDS analysis results (b, d, f) of the selected areas (in red boxes) of standard sample S1 (a, b) with Ag gridlines; (c, d) after Ag metal removal; (e, f) after glass removal.

With the Cu (with 25 wt%) added to the Ag paste, the microstructure of the Ag-Cu/Si contact is shown in Figure 2a, where the Cu and Ag metals were not uniformly mixed and the gaps at the boundary of the two materials reduced the adhesion of the gridlines. This is because Cu has higher melting point than Ag. For Ag-Cu alloy, the melting point is dependent on the Ag:Cu ratio and the lowest melting point of 778.7 ^oC can be achieved when the weight percent of Cu is 28.1 wt% [94] which is close

to the weight percent of Cu (25 wt%) in sample S2. In addition, the recrystallized interface glass was mainly found at the bottom edge of the Si pyramids with less found on the pyramids which indicates poor glass wetting during the firing.

From Figure 4.2c, after removing the metals, large amount of agglomerated Ag crystallites were found underneath the glass layer on the Si emitter and the glass was much thinner than that in the standard sample S1 as revealed in Figure 4.1c. The reduced amount of glass at the interface in S2 results from the Cu ion diffusing into the melted glass during the firing. As a result, the increased concentration of Cu ion in the glass will increase the T_g of the glass [95, 96]. What's more, from the EDS analysis in Figure 4.2d, both Pb and Te elements were not found in the recrystallized glass which is located at the top surface of Si pyramids (the red box). The reduced amount of Pb and Te was caused by two reasons: (i) less glass was completely melted and left on the emitter surface due to the increased T_g of the glass frits caused by Cu doping. (ii) the Cu-Pb and Cu-Te ion exchange reactions in the glass reduces the concentration of Pb and Te where Pb and Te elements were also related to lowering T_g of the glass [46, 47, 48, 97]. Even the Cu-Pb and Cu-Te ion exchange reactions have not been studied yet, but the mechanism should be similar to the Cu-alkali ion exchange reactions in the glass, resulting in reduced concentration of alkali ions [98]. In this case, the increased T_g of glass frits accounts for the poor glass wetting and etching of SiN_x which explains the high percent of N element in Figure 4.2h. From Figures 4.2e and 4.2g, the Ag crystallites in the Si emitter were over 700 nm in length with about 200 nm in depth, which is very close to penetrating the p-n junction [14] of which depth is about 300 nm. That is why sample S2 is exhibiting lower V_{oc} and fitted R_{sh} than S1. More so, the lower n-factor than unity shown by S2 is caused by the non-uniform wetting and etching of SiN_x by the glass in the Ag-Cu paste. Because of this non-uniform etching, the series resistance is very high and probably to the regime of impacting the V_{oc}.
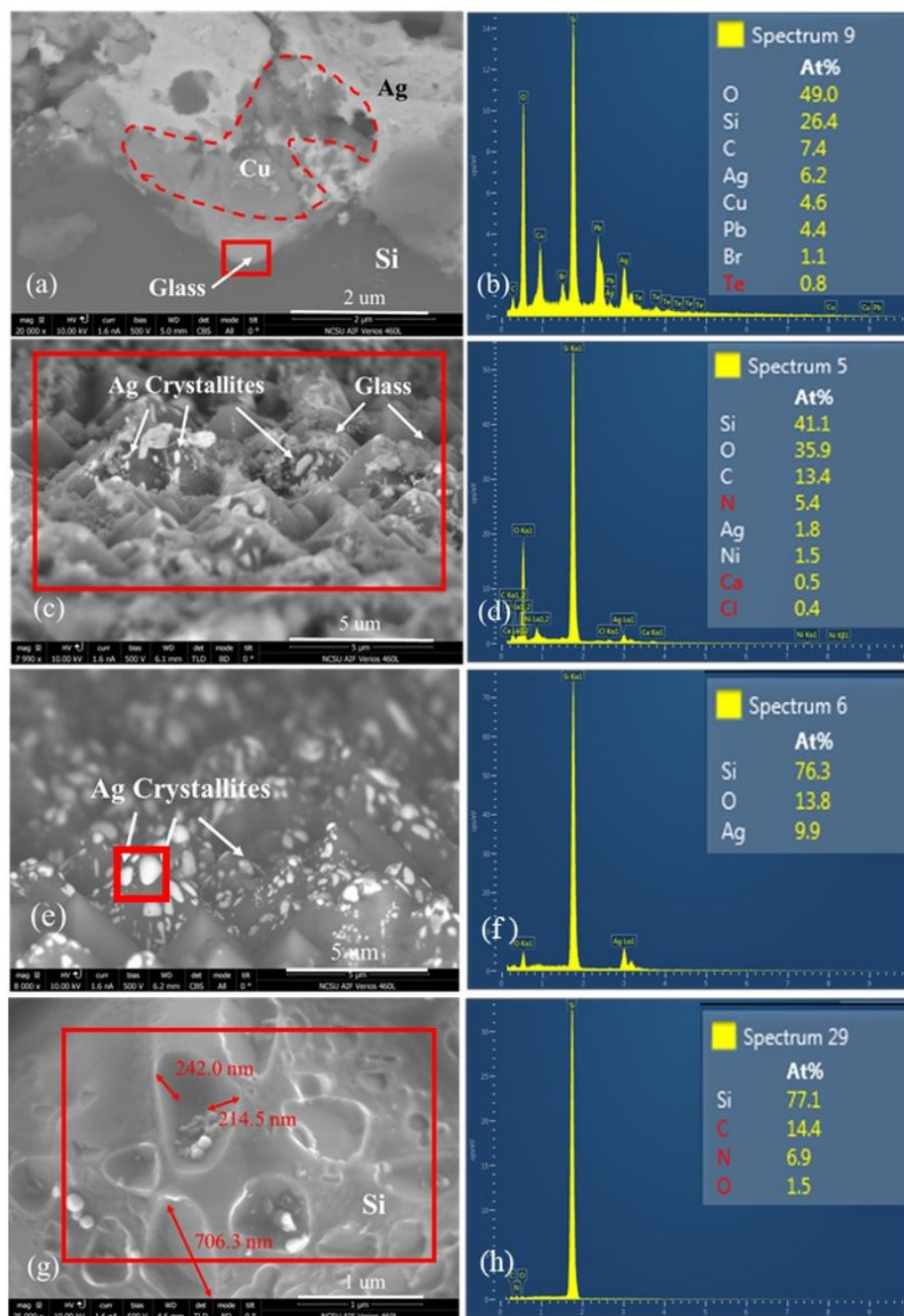
Figure 4.2: SEM images (a, c, e, g) and EDS analysis results (b, d, f, h) of the selected areas (in red boxes) of sample S2 (a, b) with Ag gridlines; (c, d) after Ag metal removal; (e, f) after glass removal; (g, h) after extra HNO3 treatment.

By increasing the amount of Cu from 25 wt% to 50 wt% in the Ag paste, the melting point of the Ag-Cu alloy increases [94], which causes poor mixture of Cu and Ag metals with large voids as shown in Figure 4.3a for sample S3. Compared

with sample S1 and S2 in Figure 4.1a and 4.2a respectively, sample S3 still has Cu particles incompletely melted and also has the melted Ag which has not aggregated. In addition, like sample S2, S3 has not enough glass on the body of the Si pyramids but some at the bottom edge. After removing the Ag-Cu gridlines, S3 had no Ag crystallites, but some fluffy glass left on the emitter which reveals that the glass was not completely melted during the firing and didn't wet the emitter surface. According to the EDS in Figure 4.3b and 4.3d where the Te element was not found in the glass and the N element is very high, the fluffy glass results from the increased T_g of glass frits due to Cu-Te ion exchange reaction, leading to reducing Te element in the glass. Thus, the glass did not completely wet and etch the SiN_x layer and there was no effective contact formed in S3, causing the lowest V_{oc}, J_{02} and the highest fitted R_{sh} in Table 4.1. Since S2 sample seems to be closer to S1, further investigation was carried out on only sample S2 to foster understanding of the contact mechanism of the Ag-Cu paste.
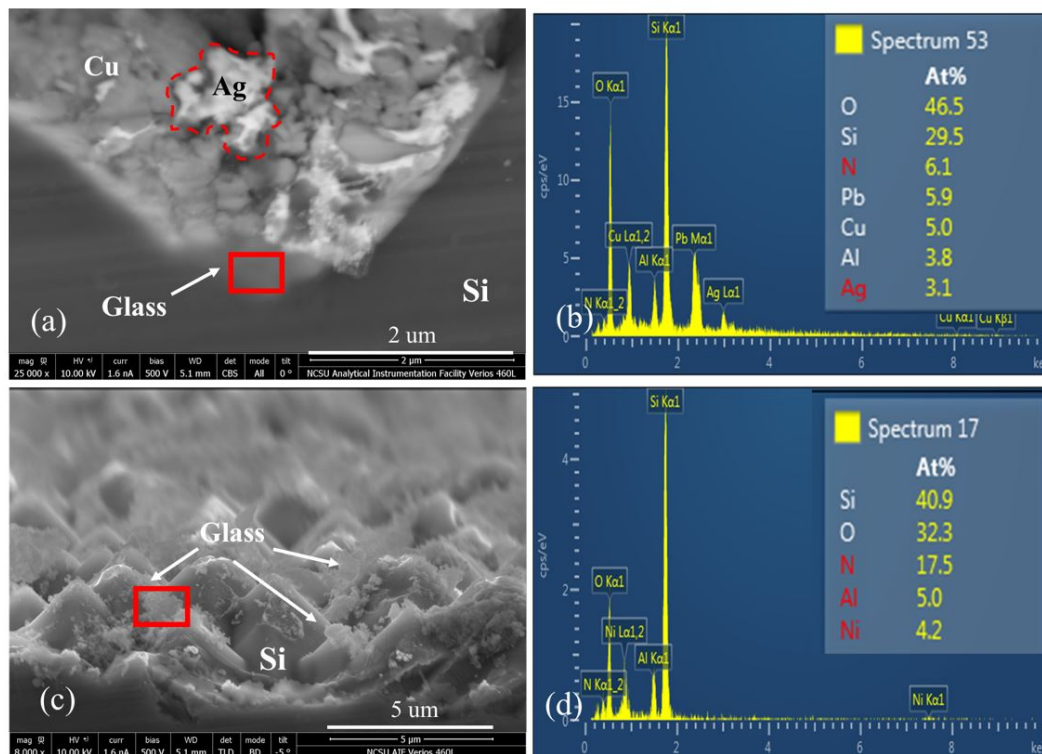
Figure 4.3: SEM images (a, c) and EDS analysis results (b, d) of the selected areas (in red boxes) of sample S3 (a, b) with Ag gridlines; (c, d) after Ag metal removal.

4.4.3   STEM and EDS Analyses

The STEM image of sample S2 is shown in Figure 4.4a with EDS analyses. After the Ag-Cu metal removal, the interface glass was thicker than 500 nm which is comparable to the standard sample S1 in Figure 4.1a. However, due to the high T_g of the glass frits because of reducing Te, Pb elements in the glass and Cu doping, the melted glass lacked enough time to wet and etch the SiN_x layer. The thickness of SiN_x layer in Figure 4.4a was around 80 nm same as the deposited thickness, which suggests that there was no etching of SiN_x. This contributes to the low V_{oc} of S2 and further confirms the SEM/EDS results of Figures 4.2d and 4.2h. In addition, Figure 4.4b shows that the Cu elements were encapsulated in the glass layer and didn't diffuse into the bulk Si, which matches with the findings of Shuichiro et al [99]. Thus, the glass layer acts as the diffusion barrier layer and prevents the Cu from diffusing into

the Si during the high temperature rapid thermal processing of Ag-Cu contact.
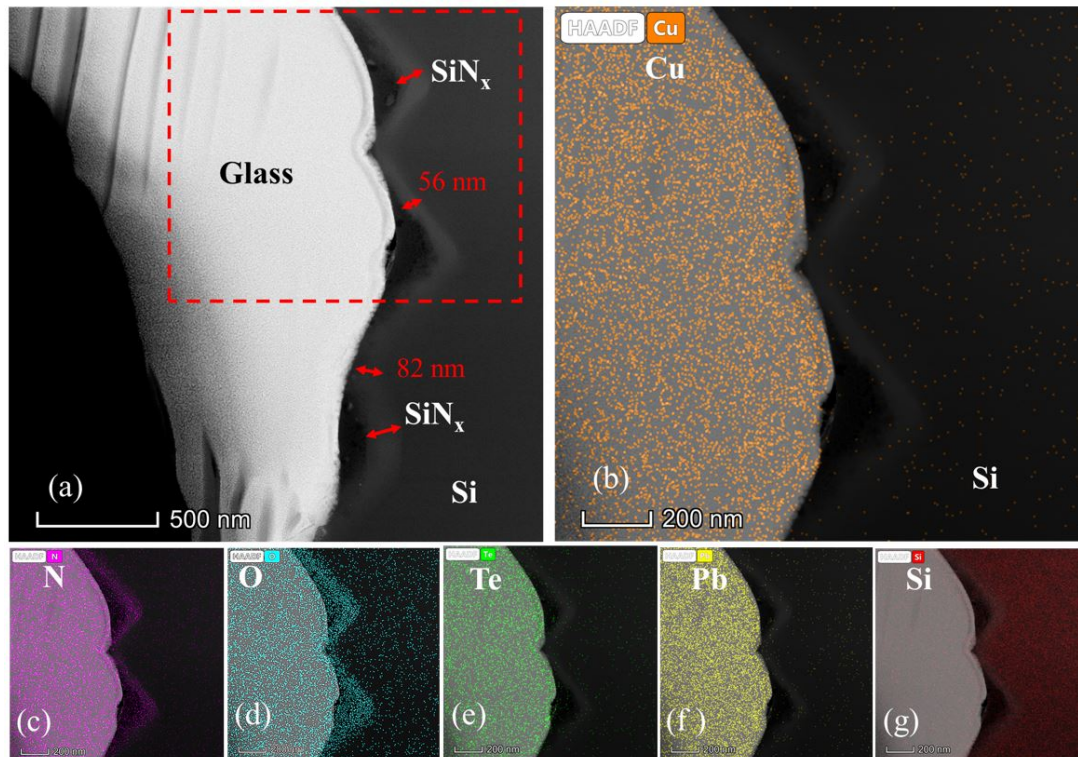
Figure 4.4: (a) STEM image of sample S2 with EDS analysis of elements: (b) Cu, (c) N, (d) O, (e) Te, (f) Pb and (g) Si.

4.4.4   Conductive-AFM

Further characterization of sample S2 used the conductive-AFM to map the current intensity on the emitter surface with and without glass layer. From Figure 4.5a, before glass removal, it has a micro-sized highly conductive area in the 3um × 3um scanning area and this conductive area was located on the body instead of the bottom of the Si pyramids according to Figure 4.5b. After the glass removal in Figure 4.5d, the micro-sized conductive areas have round or elliptical shape, and all located on the body of the Si pyramids. Based on the size, shape and the location of the conductive areas, and the SEM results in Figures 4.2e and 4.2g, these conductive areas are identified as the Ag crystallites. In addition, because of the lower current intensity of 6 nA (in Figure 4.5a) than 10 nA (in Figure 4.5d), it can be inferred that the glass layer

covering the Ag crystallites is very thin, so that the tunnelling current intensity is not reduced by the glass layer. Thus, the carrier transport mechanism in Ag-Cu/Si contact is similar to the pure Ag, which is through the Ag crystallites covered by very thin glass layer.
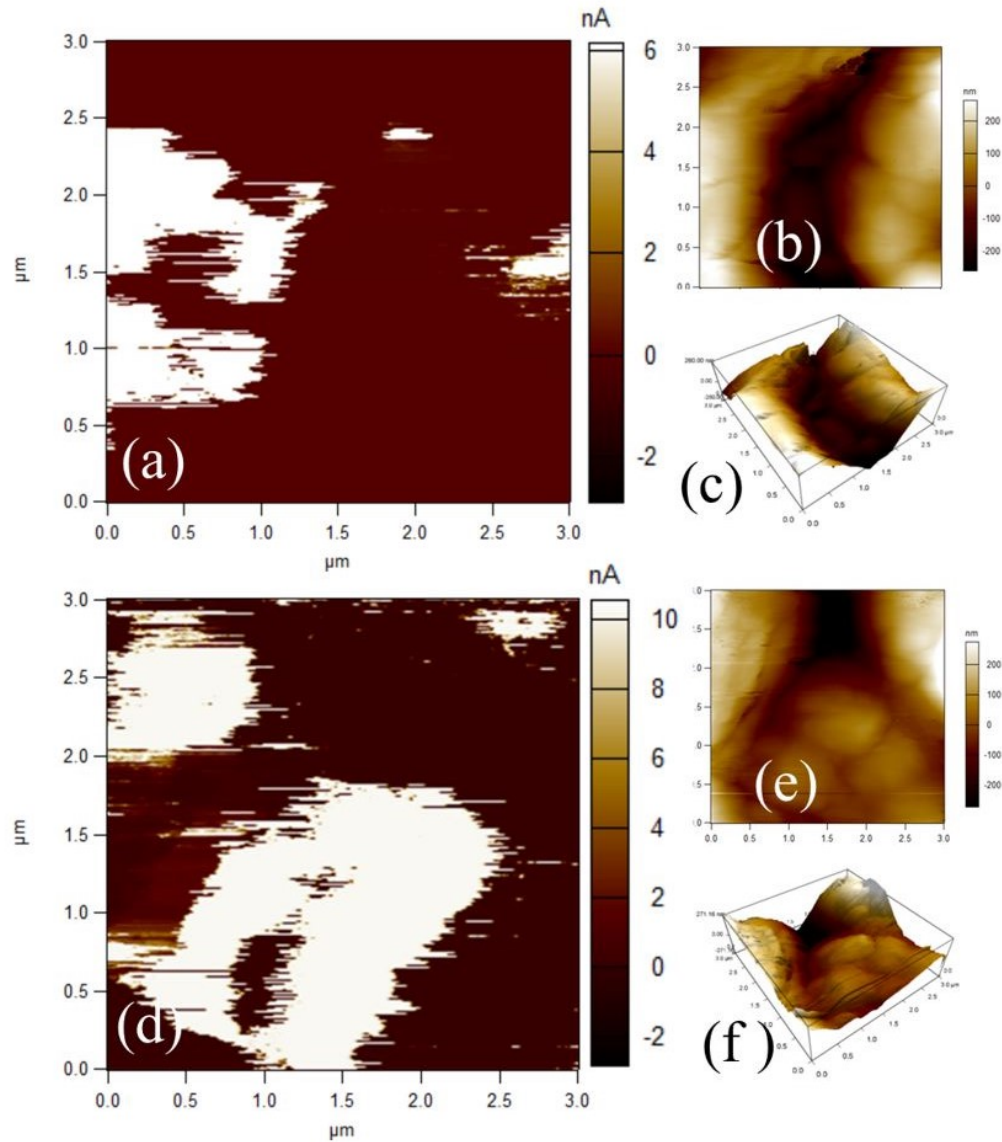
Figure 4.5: Conductive-AFM measurements on sample S2 after Ag-Cu gridlines removal (a~c) and after glass removal (d~f) according to current (a&d), height (b&e) and 3D geometry (c&f) measurement.

4.5   Conclusion

In this study, different amount of Cu (0 wt%, 25 wt%, 50 wt%) was added to the Ag paste to study the Cu diffusion during the high temperature firing in the Si solar cell. The standard sample S1 with 0 wt% Cu has the best performance with the highest V_{oc} when fired at optimal firing condition as for the commercial Ag paste. The sample S2 with 25 wt% Cu has similar J_{02} and fitted R_{sh} as S1 but lower V_{oc} and n-factor. From the SEM/EDS analyses, the Cu metal in the Ag paste can impact the Ag-Cu/Si contact through increasing the T_g of the glass frits in the paste. Thus these glass frits cannot completely melt during the rapid thermal process with poorly wetting and etching SiN_x, causing incomplete removal of SiN_x and forming large Ag crystallites on the Si pyramids. The T_g of the glass was increased by Cu doping and the reduced concentration of Te, Pb in the glass was through ion exchange reactions. Thus, the more Cu in the paste, the higher the T_g. Therefore, the sample S3 with 50 wt% Cu has the lowest V_{oc} without forming effective contact. Further investigation of Ag-Cu/Si contact on sample S2 reveals that the Te glass acts as the diffusion barrier layer and can prevent the Cu atoms from diffusing into the Si emitter during rapid thermal process. This study shows that the carrier transport mechanism in Ag-Cu/Si contact is though Ag crystallites. To achieve better metallization, the Ag-Cu paste can be further optimized through modifying the glass frits in the paste.

CHAPTER 5: Future Works

As mentioned in Chapter 4, Cu is the promising alternative metal to replace the Ag contacts for Si solar cell in order to reduce the cost. The investigation of this replacement as carried out in Chapter 4 started with the exploration of addition of Cu to Ag which resulted in the Ag-Cu contacts. This investigation showed that the reformed interface glass layer acted as a diffusion barrier layer to Cu and only the Ag crystallites were observed in the Si and confirmed that the carrier transport mechanism was through the Ag crystallites. This information was crucial to the Cu paste formulation, in particular the diffusion barrier attributes of the the interface glass layer after high temperature sintering. The Cu paste was applied in similar manner as the Ag counterpart. The Cu gridline width and height were obtained of 88 um and 67 um in Figure 5.2a and the interface characteristics is shown in Figure 5.1b. Such interface is similar to the Ag-Cu/Si interface which relies on Ag crystallites but with thicker interface glass layer. The key result here is that there was no penetration of Cu into Si as suggested by the cell LIV characteristics in Figure 5.1c as well as the microstructure in Figure 5.1b.
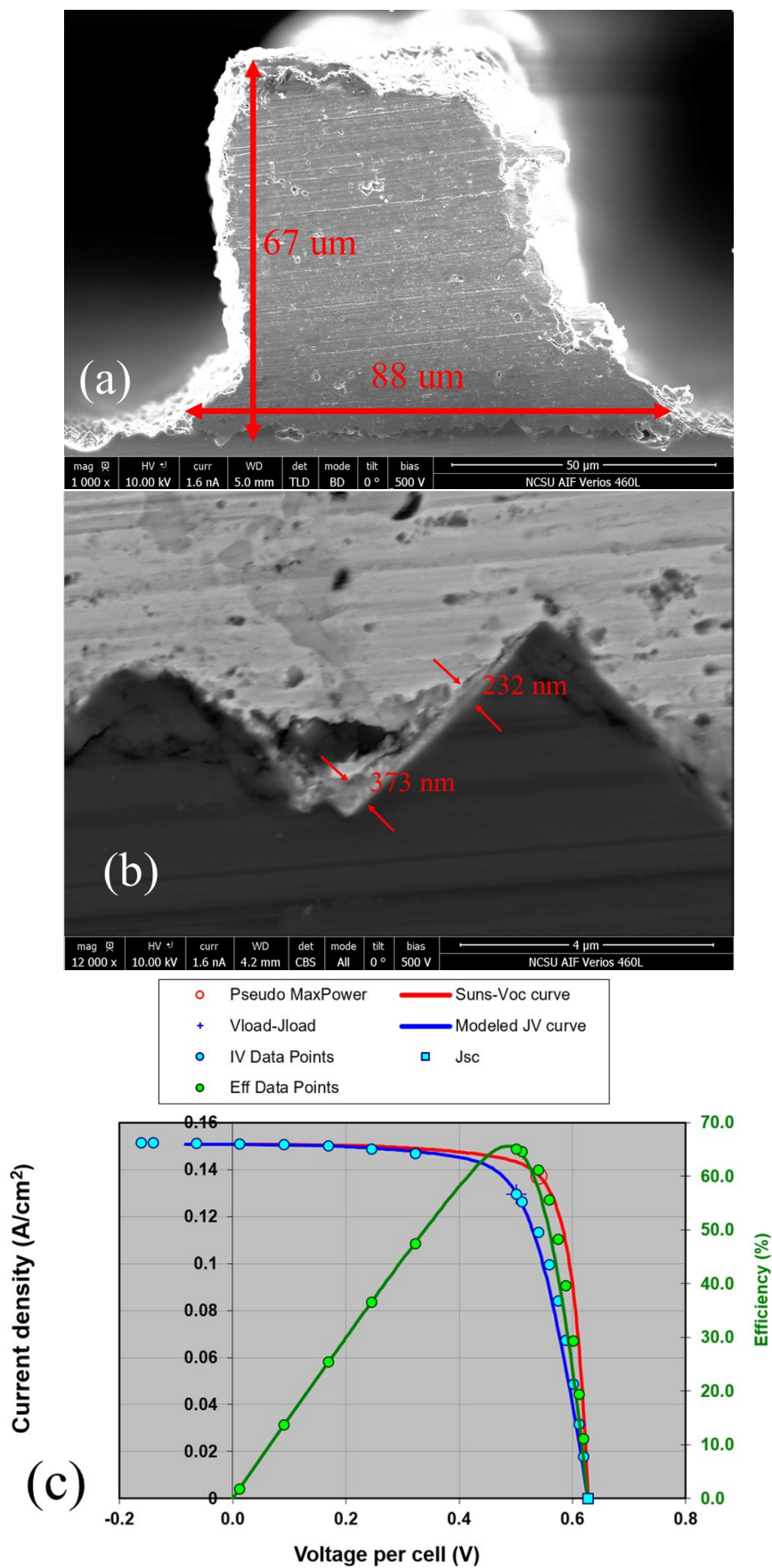
Figure 5.1: (a) SEM image of the cross section of the Cu gridline; (b) SEM image of the interface glass layer in the Cu/Si contact; (c) the LIV curve of the fabricated 5-busbars cell.

The preliminary results suggest that the Cu paste gridlines annealed at 775°C in the rapid thermal annealing furnace have Cu solids completely melt during the firing without voids, which can contribute to low gridline resistance. Comparing with the SEM image of Ag-Cu-Si contact in Figure 4.2a, this Cu paste does not exhibit the uneven mixing of Ag and Cu metals, which resulted in non-uniform etching of the SiN$_x$ and hence high contact resistance. In addition, the LIV curve of the fabricated solar cell with this Cu paste in Figure 5.1c is very promising; an open circuit voltage (V_{OC}) of 628.00 mV, short circuit current density (J_{SC}) of 36.45 mA/cm^2, fill factor (FF) of 68.70% and efficiency of 15.73%. This is comparable to the FF of the solar cells with Ag contacts in Figure 2.1c, which is $\sim$ 80%, but this Cu paste is dominated by contact resistance due to thick glass at the interface. From Figure 5.1b, the interface glass thickness ranges from 232 nm to 373 nm. Such thick glass layer would normally lead to the high contact resistance and hence the overall series resistance. Once the paste formulation is optimized, a thinner or a conductive interface glass would reach similar FF.

From this preliminary results, it is obvious that the carrier conduction mechanism for Cu/Si interface will be through a glass layer that blocks the Cu from diffusion into Si. Further characterization using conducting AFM, STEM and Raman Spectroscopy would be needed to confirm this assertion.

CHAPTER 6: CONCLUSIONS

The objectives of this dissertation are (i) to investigate the current transport mechanism through a thick interface glass layer (IGL) after contact co-firing at Ag/Si contacts on Si solar cells; (ii) to use the same techniques to investigate the transport mechanism at the Ag-Cu/Si contacts and finally (iii) the Cu-Si contacts.

(i) For the Ag/Si contacts by using the commercial pastes with Te-glass frits, the presence of Te in addition to the Pb in the paste resulted in lowering the viscosity of the molten glass during contact co-firing. This manifested in the uniform etching of the underneath silicon nitride and the formation of large nano-crystallites embedded in the glass with Ag_2Te and PbTe semimetal nanoparticles after cooling. These compounds, Ag_2Te and PbTe, have low bandgaps, and are responsible for increasing the conductivity of the glass, which enabled current to transport from the Si to the Ag gridline in spite of the glass thickness. The glass had thickness of $\geqslant$380 nm, which was measured by SEM and STEM, and was found to contain a large amount of these semimetal nanoparticles. Through modeling, based on modified Fowler-Nordheim tunneling process in conjunction with the measured c-AFM I-V characteristic curves, a barrier height of 0.1 eV and IGL thickness of $\sim$18 nm were obtained. This is contrary to the measured IGL thickness, which would result in a very high contact resistance under barrier height of 0.65 eV. However, the modeled glass thickness suggests that the presence of semimetal nanoparticles with low bandgap lowered the overall contact barrier height and increased the IGL conductivity, so that the glass thickness is inconsequential. These semimetal nanoparticles acted as a bridge to transport carriers from Si to Ag. This new carrier transport path is independent of the IGL thickness and the emitter doping concentration, which is critical to achieving

ohmic contact on the lowly doped emitter.

(ii) The second objective of this dissertation was achieved by first confirming that Cu did not diffuse into the Si during high temperature sintering. This was supported by the SEM/EDS micrograph analysis which showed that the Cu was sequestered by the oxide at the interface and Ag crystallites embedded beneath the Ag-Cu/Si interface. Thus, the carrier transport mechanism in Ag-Cu/Si contact is through Ag crystallites as with the Ag paste contact. With further optimization of the Ag-Cu paste formulation including additives, the Cu-doped glass can be conductive and transport carriers in a similar manner as seen in the Ag only contact.

(iii) The final objective of this work was to investigate the current transport mechanism at the Cu/Si contact. It is therefore possible to print and sinter Cu paste in the atmosphere without detrimental effect on solar cell. Thus, the screen-printable Cu paste applied to solar cells showed very promising electrical output parameters: V_{OC} of 628.00 mV, J_{SC} of 36.45 mA/cm^2, FF of 68.70% and efficiency of 15.73%. The low FF is caused by the high series resistance which is dominated by the high contact resistance resulting from the thick interface glass layer at the Cu/Si contact. The IGL thickness is similar to that of the Ag contact which is known to contain semimetal nanoparticles that increased the conductivity. However, with the optimization of the glass frits as in the case of commercial Ag paste, similar conductivity will be achieved in order to implement Cu-gridlines with excellent FF.

REFERENCES

[1] U. S. EIA, "Annual energy outlook 2019: with projections to 2050," 2019.

[2] "Sunshot 2030." https://www.energy.gov/eere/solar/sunshot-2030. Accessed: 2019-12-01.

[3] "Itrpv 10th edition 2019 report release and key findings." https://itrpv.vdma. org/. Accessed: 2019-12-01.

[4] K. D. Shetty, M. B. Boreland, V. Shanmugam, J. Cunnusamy, C.-K. Wu, S. Iggo, and H. Antoniadis, "Lightly doped emitters for high efficiency silicon wafer solar cells," *Energy Procedia*, vol. 33, pp. 70–75, 2013.

[5] D. K. Schroder and D. L. Meier, "Solar cell contact resistance-a review," *IEEE Transactions on electron devices*, vol. 31, no. 5, pp. 637–647, 1984.

[6] K. Varahramyan and E. Verret, "A model for specific contact resistance applicable for titanium silicide-silicon contacts," *Solid-State Electronics*, vol. 39, no. 11, pp. 1601–1607, 1996.

[7] A. M. Svensson, S. Olibet, D. Rudolph, E. Cabrera, J. Friis, K. Butler, and J. Harding, "Contact resistance of screen printed ag-contacts to si emitters: Mathematical modeling and microstructural characterization," *Journal of The Electrochemical Society*, vol. 161, no. 8, pp. E3180–E3187, 2014.

[8] A. Yu, "Electron tunneling and contact resistance of metal-silicon contact barriers," *Solid-state electronics*, vol. 13, no. 2, pp. 239–247, 1970.

[9] S. Bae, J.-W. Choi, C. Kim, S. H. Shin, H. Park, Y. Kang, H.-S. Lee, and D. Kim, "Effective contact formation method on high-sheet-resistance boron-doped emitter with current injection," *IEEE Journal of Photovoltaics*, vol. 9, no. 3, pp. 615–620, 2019.

[10] P. Kumar, M. Pfeffer, B. Willsch, and O. Eibl, "Contact formation of front side metallization in p-type, single crystalline si solar cells: Microstructure, temperature dependent series resistance and percolation model," *Solar Energy Materials and Solar Cells*, vol. 145, pp. 358–367, 2016.

[11] M. M. Hilali, S. Sridharan, C. Khadilkar, A. Shaikh, A. Rohatgi, and S. Kim, "Effect of glass frit chemistry on the physical and electrical properties of thick-film ag contacts for silicon solar cells," *Journal of electronic materials*, vol. 35, no. 11, pp. 2041–2047, 2006.

[12] S. Soo Jee, S. Yun Kim, S. Jun Kim, J. Man Park, K. Hyoung Lee, J. Ho Lee, K. Hwan Park, J. Na Heo, S. Mock Lee, I. Taek Han, *et al.*, "Enhancement of electrical conductivity of thick silver electrode using a tailored amorphous alloy," *Applied Physics Letters*, vol. 101, no. 8, p. 084104, 2012.

[13] E. Cabrera, S. Olibet, D. Rudolph, E. Wefringhaus, R. Kopecek, D. Reinke, and G. Schubert, "Influence of surface topography on the glass coverage in the contact formation of silver screen-printed si solar cells," *IEEE Journal of Photovoltaics*, vol. 3, no. 1, pp. 102–107, 2012.

[14] V. Shanmugam, A. Khanna, P. K. Basu, A. G. Aberle, T. Mueller, and J. Wong, "Impact of the phosphorus emitter doping profile on metal contact recombination of silicon wafer solar cells," *Solar Energy Materials and Solar cells*, vol. 147, pp. 171–176, 2016.

[15] E. Lohmüller, S. Werner, R. Hoenig, J. Greulich, and F. Clement, "Impact of boron doping profiles on the specific contact resistance of screen printed ag–al contacts on silicon," *Solar Energy Materials and Solar Cells*, vol. 142, pp. 2–11, 2015.

[16] W.-C. Lee and C. Hu, "Modeling cmos tunneling currents through ultrathin gate oxide due to conduction-and valence-band electron and hole tunneling," *IEEE Transactions on Electron Devices*, vol. 48, no. 7, pp. 1366–1373, 2001.

[17] H. Yang, H. Wang, X. Lei, C. Chen, and D. Cao, "Interface modeling between the printed thick-film silver paste and emitter for crystalline silicon solar cells," *International Journal of Numerical Modelling: Electronic Networks, Devices and Fields*, vol. 27, no. 4, pp. 649–655, 2014.

[18] M. Boehringer, J. Hauber, S. Passefort, and K. Eason, "In-line copper contamination monitoring using noncontact q vspv techniques," *Journal of The Electrochemical Society*, vol. 152, no. 1, pp. G1–G6, 2005.

[19] M. Polignano, D. Caputo, C. Carpanese, G. Salvà, and L. Vanzetti, "Low temperature drive-in of surface-deposited copper in silicon wafers," *The European Physical Journal Applied Physics*, vol. 27, no. 1-3, pp. 435–438, 2004.

[20] H. Vahlman, A. Haarahiltunen, W. Kwapil, J. Schon, A. Inglese, and H. Savin, "Modeling of light-induced degradation due to cu precipitation in p-type silicon. ii. comparison of simulations and experiments," *Journal of Applied Physics*, vol. 121, no. 19, p. 195704, 2017.

[21] Y. R. Cheng, W. J. Chen, K. Ohdaira, and K. Higashimine, "Barrier properties of electroplating nickel layer for copper metallization in silicon solar cells," *Int. J. Electrochem. Sci*, vol. 13, p. 11516, 2018.

[22] C. H. Hsiao, J. Y. Wu, and W. J. Chen, "Adhesion strength of plated ni/cu metallization in si solar cells," *Journal of Materials Science: Materials in Electronics*, vol. 30, no. 4, pp. 3539–3544, 2019.

[23] C.-L. Cheng, C.-C. Liu, and C.-T. Yeh, "Photovoltaic and physical characteristics of screen-printed monocrystalline silicon solar cells with laser doping and electroplated copper," *International Journal of Photoenergy*, vol. 2019, 2019.

[24] N. Balaji, M. C. Raval, and S. Saravanan, "Review on metallization in crystalline silicon solar cells," in *Solar Cells*, IntechOpen, 2019.

[25] M. Mebarki and A. Layadi, "Investigation of the physical properties of fe/si for use in a cu/fe/si solar cells contact," *Materials Research Express*, vol. 6, no. 11, p. 115505, 2019.

[26] "Sunshot 2030." https://www.energy.gov/eere/solar/sunshot-2030. Accessed: 2019-10-14.

[27] W. Shockley and H. J. Queisser, "Detailed balance limit of efficiency of p-n junction solar cells," *Journal of applied physics*, vol. 32, no. 3, pp. 510–519, 1961.

[28] M. Fischer, "Itrpv 9th edition 2018 report release and key findings," in *PV Cell-Tech conference*, 2018.

[29] K. H. Kim, C. S. Park, J. D. Lee, J. Y. Lim, J. M. Yeon, I. H. Kim, E. J. Lee, and Y. H. Cho, "Record high efficiency of screen-printed silicon aluminum back surface field solar cell: 20.29%," *Japanese Journal of Applied Physics*, vol. 56, no. 8S2, p. 08MB25, 2017.

[30] W. Deng, F. Ye, R. Liu, Y. Li, H. Chen, Z. Xiong, Y. Yang, Y. Chen, Y. Wang, P. P. Altermatt, *et al.*, "22.61% efficient fully screen printed perc solar cell," in *2017 IEEE 44th Photovoltaic Specialist Conference (PVSC)*, pp. 2220–2226, IEEE, 2017.

[31] B. Voss, T. Knobloch, and A. Goetzberger, "Crystalline silicon solar cells," 1998.

[32] C. Ballif, D. Huljić, G. Willeke, and A. Hessler-Wyser, "Silver thick-film contacts on highly doped n-type silicon emitters: structural and electronic properties of the interface," *Applied physics letters*, vol. 82, no. 12, pp. 1878–1880, 2003.

[33] N. Chen and A. Ebong, "Towards 20% efficient industrial al-bsf silicon solar cell with multiple busbars and fine gridlines," *Solar Energy Materials and Solar Cells*, vol. 146, pp. 107–113, 2016.

[34] N. Chen, K. Tate, and A. Ebong, "Generalized analysis of the impact of emitter sheet resistance on silicon solar cell performance," *Japanese Journal of Applied Physics*, vol. 54, no. 8S1, p. 08KD20, 2015.

[35] F. Ye, D. Weiwei, D. Chen, Y. Chen, D. Jianwen, J. Ding, N. Yuan, Z. Feng, and P. Verlinden, "The influence of a low doping concentration emitter on the performance of selective emitter silicon solar cells," 09 2014.

[36] G. Grupp, D. Huljic, R. Preu, G. Willeke, and J. Luther, "Peak firing temperature dependence of the microstructure of ag thick-film contacts on silicon solar cells-a detailed afm study of the interface," *Proc. 20th EC PVSEC*, 2005.

[37] S. Kontermann, G. Willeke, and J. Bauer, "Electronic properties of nanoscale silver crystals at the interface of silver thick film contacts on n-type silicon," *Applied Physics Letters*, vol. 97, no. 19, p. 191910, 2010.

[38] S. Kontermann, R. Preu, and G. Willeke, "Calculating the specific contact resistance from the nanostructure at the interface of silver thick film contacts on n-type silicon," *Applied Physics Letters*, vol. 99, no. 11, p. 111905, 2011.

[39] Z. Li, L. Liang, and L. Cheng, "Electron microscopy study of front-side ag contact in crystalline si solar cells," 2009.

[40] P. Kumar, M. Pfeffer, B. Willsch, O. Eibl, L. J. Koduvelikulathu, V. D. Mihailetchi, and R. Kopecek, "N-type single-crystalline si solar cells: Front side metallization for solar cells reaching 20% efficiency," *Solar Energy Materials and Solar Cells*, vol. 157, pp. 200–208, 2016.

[41] A. Rohatgi, M. M. Hilali, D. Meier, A. Ebong, C. B. Honsberg, A. Carroll, and P. Hacke, "Self-aligned self-doping selective emitter for screen-printed silicon solar cells," Georgia Institute of Technology, 2001.

[42] M. M. Hilali, M. M. Al-Jassim, B. To, H. Moutinho, A. Rohatgi, and S. Asher, "Understanding the formation and temperature dependence of thick-film ag contacts on high-sheet-resistance si emitters for solar cells," *Journal of the Electrochemical Society*, vol. 152, no. 10, pp. G742–G749, 2005.

[43] L. Liang, Z. Li, L. Cheng, N. Takeda, and A. Carroll, "Microstructural characterization and current conduction mechanisms of front-side contact of n-type crystalline si solar cells with ag/al pastes," *Journal of Applied Physics*, vol. 117, no. 21, p. 215102, 2015.

[44] W.-H. Lee, T.-K. Lee, and C.-Y. Lo, "Environmentally-friendly, pb-free cu front electrode for si-based solar cell applications," *Journal of Alloys and Compounds*, vol. 686, pp. 339–346, 2016.

[45] J. Jiang, Y. He, Z. Zhang, J. Wei, and L. Li, "Pb-free front-contact silver pastes with snop2o5 glass frit for crystalline silicon solar cells," *Journal of Alloys and Compounds*, vol. 689, pp. 662–668, 2016.

[46] X.-X. Pi, X.-H. Cao, Z.-X. Fu, L. Zhang, P.-D. Han, L.-X. Wang, and Q.-T. Zhang, "Application of te-based glass in silicon solar cells," *Acta Metallurgica Sinica (English Letters)*, vol. 28, no. 2, pp. 223–229, 2015.

[47] J. Qin, W. Zhang, S. Bai, and Z. Liu, "Effect of pb–te–o glasses on ag thick-film contact in crystalline silicon solar cells," *Solar Energy Materials and Solar Cells*, vol. 144, pp. 256–263, 2016.

[48] G. Zheng, Y. Tai, H. Wang, and J. Bai, "Effect of the pb–te–b–o system glass frits in the front contact paste on the conversion efficiency of crystalline silicon

solar cells," *Journal of Materials Science: Materials in Electronics*, vol. 25, no. 9, pp. 3779–3786, 2014.

[49] F. Ming, C. Si-Guo, W. Yue, Z. Hong, and F. Lin, "Effects of te-bi glass frit on performances of front silver contacts for crystalline silicon solar cells," *JOURNAL OF INORGANIC MATERIALS*, vol. 31, no. 8, pp. 785–790, 2016.

[50] H. Wang, S. Ma, Q. Ma, X. Cheng, H. Wang, and J. Bai, "Effect of composition of front-electrode-paste glass on electrical performance of multicrystalline silicon solar cells," *Journal of Materials Science: Materials in Electronics*, vol. 28, no. 9, pp. 6936–6949, 2017.

[51] M. Kurahashi, N. Shindo, K. Nishimura, K. Shirasawa, and H. Takato, "Investigation of the reaction mechanisms of lead-free and bismuth-free tellurite glass in front silver paste for c-si solar cells," in *2018 IEEE 7th World Conference on Photovoltaic Energy Conversion (WCPEC)(A Joint Conference of 45th IEEE PVSC, 28th PVSEC & 34th EU PVSEC)*, pp. 1033–1036, IEEE, 2018.

[52] A. Qin, Y. Fang, P. Tao, J. Zhang, and C. Su, "Silver telluride nanotubes prepared by the hydrothermal method," *Inorganic chemistry*, vol. 46, no. 18, pp. 7403–7409, 2007.

[53] T. Milenov, T. Tenev, I. Miloushev, G. Avdeev, C. Luo, and W. Chou, "Preliminary studies of the raman spectra of ag2te and ag5te3," *Optical and Quantum Electronics*, vol. 46, no. 4, pp. 573–580, 2014.

[54] B. Zhang, C. Cai, H. Zhu, F. Wu, Z. Ye, Y. Chen, R. Li, W. Kong, and H. Wu, "Phonon blocking by two dimensional electron gas in polar cdte/pbte heterojunctions," *Applied Physics Letters*, vol. 104, no. 16, p. 161601, 2014.

[55] K. Ren, V. Unsur, A. Chowdhury, Y. Zhang, and A. Ebong, "The impact of tellurite glass on contact resistance of the fire through dielectric (ftd) c-si solar cell with lightly doped emitter," in *2018 IEEE 7th World Conference on Photovoltaic Energy Conversion (WCPEC)(A Joint Conference of 45th IEEE PVSC, 28th PVSEC & 34th EU PVSEC)*, pp. 1051–1054, IEEE, 2018.

[56] R. Hoenig, M. Duerrschnabel, W. van Mierlo, Z. Aabdin, J. Bernhard, J. Biskupek, O. Eibl, U. Kaiser, J. Wilde, F. Clement, *et al.*, "The nature of screen printed front side silver contacts-results of the project mikrosol," *Energy Procedia*, vol. 43, pp. 27–36, 2013.

[57] E. Cabrera, S. Olibet, J. Glatz-Reichenbach, R. Kopecek, D. Reinke, and G. Schubert, "Experimental evidence of direct contact formation for the current transport in silver thick film metallized silicon emitters," *Journal of Applied Physics*, vol. 110, no. 11, p. 114511, 2011.

[58] D. Kim, S. Hwang, and H. Kim, "Effect of the thermal properties of frits on the electrical properties of screen-printed silicon solar cells," *Journal of the Korean Physical Society*, vol. 55, no. 3, pp. 1046–1050, 2009.

[59] S. Watanabe, T. Kodera, and T. Ogihara, "Influence of tellurite glass on reaction between si3n4 anti-reflection coating film and ag paste for electrodes in si solar cells," *Journal of the Ceramic Society of Japan*, vol. 124, no. 3, pp. 218–222, 2016.

[60] S.-B. Cho, K.-K. Hong, J.-Y. Huh, H. J. Park, and J.-W. Jeong, "Role of the ambient oxygen on the silver thick-film contact formation for crystalline silicon solar cells," *Current Applied Physics*, vol. 10, no. 2, pp. S222–S225, 2010.

[61] C.-H. Lin, S.-Y. Tsai, S.-P. Hsu, and M.-H. Hsieh, "Investigation of ag-bulk/glassy-phase/si heterostructures of printed ag contacts on crystalline si solar cells," *Solar Energy Materials and Solar Cells*, vol. 92, no. 9, pp. 1011–1015, 2008.

[62] Z. Li, L. Liang, A. Ionkin, B. Fish, M. Lewittes, L. Cheng, and K. Mikeska, "Microstructural comparison of silicon solar cells' front-side ag contact and the evolution of current conduction mechanisms," *Journal of applied Physics*, vol. 110, no. 7, p. 074304, 2011.

[63] H. Nakatsuji, A. Shimizu, and Y. Omura, "Semi-empirical and practical model for low-electric field direct tunneling current estimation in nanometer-thick sio2films," *Superlattices and Microstructures*, vol. 28, no. 5-6, pp. 425–428, 2000.

[64] K. Ren, T. Ye, Y. Zhang, and A. Ebong, "The role of nano-crystallites on conduction mechanisms of current through ag gridlines of si solar cells," *MRS Advances*, vol. 4, no. 5-6, pp. 311–318, 2019.

[65] K. Ren, D. Han, and A. Ebong, "Electrical characterization of nano-colloids in si solar cell screen-printed contacts by conductive atomic force microscopy (c-afm)," in *36th EU PVSEC proceedings*, 2019.

[66] D. Xu, G. D. Watt, J. N. Harb, and R. C. Davis, "Electrical conductivity of ferritin proteins by conductive afm," *Nano letters*, vol. 5, no. 4, pp. 571–577, 2005.

[67] W. Frammelsberger, G. Benstetter, J. Kiely, and R. Stamp, "Thickness determination of thin and ultra-thin sio2 films by c-afm iv-spectroscopy," *Applied Surface Science*, vol. 252, no. 6, pp. 2375–2388, 2006.

[68] W. Frammelsberger, G. Benstetter, J. Kiely, and R. Stamp, "C-afm-based thickness determination of thin and ultra-thin sio2 films by use of different conductive-coated probe tips," *Applied Surface Science*, vol. 253, no. 7, pp. 3615–3626, 2007.

[69] R. Balsano, A. Matsubayashi, and V. P. LaBella, "Schottky barrier height measurements of cu/si (001), ag/si (001), and au/si (001) interfaces utilizing ballistic electron emission microscopy and ballistic hole emission microscopy," *AIP Advances*, vol. 3, no. 11, p. 112110, 2013.

[70] K. Ahn, C. Li, C. Uher, and M. G. Kanatzidis, "Improvement in the thermoelectric figure of merit by la/ag cosubstitution in pbte," *Chemistry of Materials*, vol. 21, no. 7, pp. 1361–1367, 2009.

[71] P. Rawat, B. Paul, and P. Banerji, "Lead telluride based thermoelectrics: approaches for higher efficiency," 2013.

[72] F. Aliev, E. Kerimova, and S. Aliev, "Electrical and thermoelectric properties of p-ag 2 te," *Semiconductors*, vol. 36, no. 8, pp. 869–873, 2002.

[73] M. Jafarov, F. Aliev, R. Hasanova, and A. Saddinova, "Role of intrinsic defects in splitting the energy spectra of charge carriers in ag 2 te," *Semiconductors*, vol. 46, no. 7, pp. 861–865, 2012.

[74] M. Bala, S. Gupta, T. Tripathi, D. Avasthi, and K. Asokan, "Effect of ag doping and annealing on thermoelectric properties of pbte," in *AIP Conference Proceedings*, vol. 1665, p. 110047, AIP Publishing, 2015.

[75] S. Aliev and F. Aliev, "Electronic processes in vicinity of structural phase transformation in ag 2 te and ag 2 se," *Izvestiya Akademii Nauk SSSR, Neorganicheskie Materialy*, vol. 25, no. 2, pp. 241–246, 1989.

[76] T. Li and W. A. Schroeder, "Pbte (111) sub-thermionic photocathode: A route to high-quality electron pulses," *arXiv preprint arXiv:1704.00194*, 2017.

[77] S. Kashida, N. Watanabe, T. Hasegawa, H. Iida, and M. Mori, "Electronic structure of ag2te, band calculation and photoelectron spectroscopy," *Solid State Ionics*, vol. 148, no. 1-2, pp. 193–201, 2002.

[78] I. C. Urbiola, R. R. Bon, and Y. Vorobiev, "Lead telluride through transformation of plumbonacrite in tellurium atmosphere and its behavior as part of pbte–si photodiode," *IEEE Sensors Journal*, vol. 16, no. 15, pp. 5875–5882, 2016.

[79] H. Yang, J.-H. Bahk, T. Day, A. M. Mohammed, G. J. Snyder, A. Shakouri, and Y. Wu, "Enhanced thermoelectric properties in bulk nanowire heterostructure-based nanocomposites through minority carrier blocking," *Nano letters*, vol. 15, no. 2, pp. 1349–1355, 2015.

[80] S. H. Lee, D. W. Lee, and S. H. Lee, "Review of conductive copper paste for c-si solar cells," *Korean Journal of Metals and Materials*, vol. 55, no. 9, pp. 637–644, 2017.

[81] "Historical copper spot price chart." https://www.providentmetals.com/spot-price/chart/copper/. Accessed: 09-20-2019.

[82] "Historical silver spot price chart." https://www.providentmetals.com/spot-price/chart/silver/. Accessed: 09-20-2019.

[83] A. A. Istratov and E. R. Weber, "Physics of copper in silicon," *Journal of The Electrochemical Society*, vol. 149, no. 1, pp. G21–G30, 2002.

[84] C. Modanese, M. Wagner, F. Wolny, A. Oehlke, H. Laine, A. Inglese, H. Vahlman, M. Yli-Koski, and H. Savin, "Impact of copper on light-induced degradation in czochralski silicon perc solar cells," *Solar Energy Materials and Solar Cells*, vol. 186, pp. 373–377, 2018.

[85] S. Adachi, T. Kato, T. Aoyagi, T. Naito, H. Yamamoto, T. Nojiri, Y. Kurata, Y. Kurihara, and M. Yoshida, "Development of innovative application films for silicon solar cells using a copper–phosphorus alloy by an atmospheric sintering process," *IEEE Journal of Photovoltaics*, vol. 3, no. 4, pp. 1178–1183, 2013.

[86] P. Vitanov, N. Tyutyundzhiev, P. Stefchev, and B. Karamfilov, "Low cost multilayer metallization system for silicon solar cells," *Solar energy materials and solar cells*, vol. 44, no. 4, pp. 471–484, 1996.

[87] E.-J. Lee, D. Kim, and S. Lee, "Ni/cu metallization for low-cost high-efficiency perc cells," *Solar energy materials and solar cells*, vol. 74, no. 1-4, pp. 65–70, 2002.

[88] J. Kang, J. You, C. Kang, J. J. Pak, and D. Kim, "Investigation of cu metallization for si solar cells," *Solar energy materials and solar cells*, vol. 74, no. 1-4, pp. 91–96, 2002.

[89] J. You, J. Kang, D. Kim, J. J. Pak, and C. S. Kang, "Copper metallization for crystalline si solar cells," *Solar energy materials and solar cells*, vol. 79, no. 3, pp. 339–345, 2003.

[90] G. Dapei, G. Papadimitropoulos, D. Varvitsiotis, G. Koustas, M. Vasilopoulou, and D. Davazoglou, "Screen-printed copper for front-and back-side metallization of single-and multi-crystalline silicon solar cells," *physica status solidi (a)*, vol. 212, no. 12, pp. 2816–2821, 2015.

[91] M. A. Green, "Ag requirements for silicon wafer-based solar cells," *Progress in Photovoltaics: Research and Applications*, vol. 19, no. 8, pp. 911–916, 2011.

[92] A. Skwarek, K. Drabczyk, and R. P. Socha, "Copper deposition on screen printed electrical paths for solar cell application," *Circuit World*, 2015.

[93] D. Wood, I. Kuzma-Filipek, R. Russell, F. Duerinckx, N. Powell, A. Zambova, B. Chislea, P. Chevalier, C. Boulord, A. Beucher, *et al.*, "Passivated busbars from screen-printed low-temperature copper paste," *Energy Procedia*, vol. 55, pp. 724–732, 2014.

[94] P. Subramanian and J. Perepezko, "The ag-cu (silver-copper) system," *Journal of Phase Equilibria*, vol. 14, no. 1, pp. 62–75, 1993.

[95] E. A. Neel, I. Ahmed, J. Pratten, S. Nazhat, and J. Knowles, "Characterisation of antibacterial copper releasing degradable phosphate glass fibres," *Biomaterials*, vol. 26, no. 15, pp. 2247–2254, 2005.

[96] G. Duan, D. Xu, and W. L. Johnson, "High copper content bulk glass formation in bimetallic cu-hf system," *Metallurgical and Materials Transactions A*, vol. 36, no. 2, pp. 455–458, 2005.

[97] M. Fu, S.-G. Cheng, Y. Wang, H. ZHOU, and L. FAN, "Effects of te-bi glass frit on performances of front silver contacts for crystalline silicon solar cells," *J. Inorg. Mater*, vol. 31, p. 785, 2016.

[98] F. Gonella, F. Caccavale, L. Bogomolova, F. d'Acapito, and A. Quaranta, "Experimental study of copper-alkali ion exchange in glass," *Journal of applied physics*, vol. 83, no. 3, pp. 1200–1206, 1998.

[99] S. Adachi, T. Nojiri, T. Kato, S. Watanabe, and M. Yoshida, "Atmospherically sintered copper-base alloy application film with self-assembled barrier layer on silicon substrate for silicon photovoltaics," *Journal of Alloys and Compounds*, vol. 757, pp. 333–339, 2018.